Petroleum Science 23 (2026) 1588–1605

Contents lists available at ScienceDirect

Petroleum Science

journal homepage: www.keaipublishing.com/en/journals/petroleum-science

Original Paper

Unlocking the seal capacity of unconsolidated Quaternary hydrate-bearing sediments: Carbon isotope gradients as a proxy for dynamic gas trapping efficiency

Ya-Zhou Liu [a,b,c,*], Jian-Hui Zeng [a,b,c], Jun-Cheng Qiao [a,b,c,**], Gui-Wen Wang [a,b,c], Ke-Liang Dong [a,b,c], Shu-Ning Liu [a,b,c]

[a] State Key Laboratory of Petroleum Resources and Engineering, China University of Petroleum (Beijing), Beijing, 102249, China
[b] College of Geosciences, China University of Petroleum (Beijing), Beijing, 102249, China
[c] Hainan Institute of China University of Petroleum (Beijing), Sanya, 572025, Hainan, China

ARTICLE INFO

Article history:
Received 5 July 2025
Received in revised form
8 October 2025
Accepted 4 December 2025
Available online 9 December 2025

Edited by Min Li

Keywords:
Seal capacity
Unconsolidated hydrate-bearing sediments
Carbon isotope gradients
Accumulation model
Qiongdongnan Basin

ABSTRACT

Submarine gas hydrate systems store vast carbon inventories (~1500–12,400 Gt C) yet pose dual risks as potential geohazard multipliers and climate feedback agents under oceanic warming. Conventional seal assessment fails catastrophically in unconsolidated Quaternary hydrate-bearing sediments due to core-retrieval artifacts, hydrate morphology controls on capillary trapping, and meter-scale heterogeneity unresolved by seismic methods. Here, we pioneer methane carbon isotope ($\delta^{13}C_1$) gradients as a dynamic proxy for seal capacity in the Qiongdongnan Basin. Integrating petrographic features, natural gas geochemical characteristics, downhole logging data, and principal component analysis (PCA) from six wells, we: (1) quantified the thermogenic gas contribution of wells W6 and W8 to be 55%–73%, and that of well W1 to be 28%–32% via binary mixing models, (2) establish that methane carbon isotope gradients >0.5‰/m diagnose effective capillary barriers, correlating with zones of pore-throat disconnection, and (3) develop a PCA-integrated logging model (cumulative variance: 84.02%, $R^2 = 0.78$) predicting seal capacity from conventional petrophysical parameters. Furthermore, the results validate a charge-dynamic barrier-mixing accumulation model where thermogenic gas influx elevates hydrate saturation, creating self-sealing horizons that trap underlying microbial gases and subsequently charged thermogenic gases, recorded in diagnostic methane carbon isotope reversals. This approach bridges molecular-scale fractionation and reservoir-scale processes, enabling targeted identification of high-integrity seals for optimized carbon storage and safer hydrate exploitation in rapidly deposited marginal basins.

1. Introduction

The accelerating climate crisis demands innovative strategies to simultaneously mitigate atmospheric CO_2 levels and decarbonize energy systems, placing submarine gas hydrate systems at the epicenter of geoscientific urgency. These frozen methane reservoirs store ~1500–12,400 Gt (gigatons) of carbon—surpassing global conventional gas reserves by an order of magnitude (Ruppel and Kessler, 2017; IEA, 2024)—yet their dual role as potential "geohazard multipliers" and "transitional energy sources" remains unresolved. Recent industrial breakthroughs in ultra-deepwater basins (e.g., China's Lingshui 36-1 field holding >100 Bcm gas at <500 m burial, Xu et al., 2025; India's Krishna-Godavari hydrate production test, 2024) demonstrate the technical viability of shallow-gas resourceization, aligning with IPCC's (Intergovernmental Panel on Climate Change) mandate for low-carbon fossil fuel bridging during energy transitions. Critically, however, hydrate dissociation triggered by oceanic warming (0.12 °C/decade at 500 m depth, Ruppel, 2011) could release 4–25 Gt CH_4/

* Corresponding author.
** Corresponding author.
E-mail addresses: maxliuyzh@163.com (Y.-Z. Liu), Juncheng.Qiao@cup.edu.cn (J.-C. Qiao).

Peer review under the responsibility of China University of Petroleum (Beijing).

https://doi.org/10.1016/j.petsci.2025.12.008

century—equivalent to 100–500 years of current anthropogenic emissions—amplifying climate feedback loops through abrupt methane pulses (Marín-Moreno et al., 2013, 2015; Dean et al., 2018). This existential dichotomy underscores a global imperative: developing predictive metrics to quantify dynamic seal integrity in hydrate-bearing sediments for concurrent carbon sequestration and geohazard-neutralized gas extraction.

Conventional seal assessment fails catastrophically in unconsolidated Quaternary strata, where hydrate morphology dictates pore-scale fluid trapping but evades traditional petrophysical characterization. Standard methods relying on core-derived capillary pressure (e.g., mercury injection) and permeability measurements suffer from irreducible artifacts: hydrate dissociation during retrieval alters sediment fabric (Sellm and Sloan, 1990; Feng et al., 2023; Yoshimoto et al., 2023), while drilling-induced remolding obliterates metastable grain contacts (Passchier, 2000; H.Y. Zhu et al., 2021). Even advanced seismic indicators (BSRs, amplitude blanking) lack the resolution to diagnose meter-scale seal heterogeneities where >90% of slope failures initiate (Bray and Macedo, 2023; Kong et al., 2025). Compounding this, hydrate growth habit—whether pore-filling, load-bearing, or cementing—exerts first-order control on breakthrough pressure (varying by 300%–800%; Sun et al., 2022; Zhao et al., 2023), but remains invisible to well logs and basin models. Consequently, existing frameworks cannot resolve why some hydrate layers trap gigascale gas columns (e.g., Nankai Trough's 100 Bcm accumulation) while others catastrophically fail, triggering events like the Storegga Slide that released 104–504 Gt CO_2-equivalent methane (Archer, 2007; Brook et al., 2008). This knowledge gap represents a fundamental Earth system process blind spot, impeding both IPCC's "Blue Carbon" sequestration agenda and UNISDR's (United Nations Office for Disaster Risk Reduction) geohazard mitigation goals.

Here, we pioneer methane carbon isotope gradients as a geochemical proxy for dynamic seal capacity. Integrating downhole logging, geochemical profiling and analytical data, and principal component analysis (PCA), we establish a quantitative framework that: (1) deciphers thermogenic vs. biogenic methane contributions in mixed-source systems, (2) correlates isotopic discontinuities with capillary barrier strength, and (3) resolves transient gas trapping in hydrate-bearing sequences. Using the Qiongdongnan Basin as a natural laboratory, we demonstrate that peak gradients >0.5‰/m diagnose effective seals where traditional petrophysics fails. Our approach bridges molecular-scale fractionation processes and basin-scale carbon budgets, ultimately enabling predictive mapping of seal integrity for optimized carbon storage and safer gas hydrate exploitation.

2. Geological setting

The Qiongdongnan Basin (QDNB) is a Cenozoic rift basin on the continental margin of the northern South China Sea (Fig. 1(a)), with an area of approximately 8.3×10^4 km^2 (Cao et al., 2022; Liu et al., 2023). The QDNB is adjacent to the Hainan Uplift in the north, and the Xisha Uplift in the south, and is sandwiched between the Pearl River Mouth Basin (PRMB) and the Yinggehai Basin (YGHB) in the east and west (Fig. 1(c)). It is an important deep-water (water depth greater than 1000 m) hydrocarbon resource exploration area in the northern part of the South China Sea (Xu et al., 2025; Zhang et al., 2025). From north to south, it can be further divided into four tectonic units: the northern depression zone (Songtao and Yacheng Sags), the central uplift zone (Songtao, Lingshui and Yacheng Uplifts), the central depression zone (Songnan, Lingshui, Ledong, Changchang, Baodao, and Beijiao Sags) and the southern uplift zone (Cao et al., 2022). Since the Paleocene, the QDNB has experienced syn-rifting and post-rifting periods due to the interaction between the Pacific Plate and the Eurasian Plate and the seafloor spreading in the South China Sea, bounded by the regional unconformity T60 (23 Ma) (Fig. 1(b)) (Zhang et al., 2021).

Supplied by sediments from Hainan Island, Vietnam, and the Red River system, the sediment-fill sequence of the QDNB contains up to 8 km of clastic sediments ranging in age from the Paleogene to the Quaternary (Su et al., 2023). Coal in the Oligocene Lingshui and Yacheng Formations is the main gas-prone source rock (Fig. 1(b)) (Xiao et al., 2006). The sandstone units deposited in the Lingshui, Sanya, and Huangliu Formations are potential reservoirs. The thick mudstones of the Late Miocene Huangliu Formation and the Pliocene Yinggehai Formation provide an excellent regional seal for hydrocarbon accumulation. The Quaternary Ledong Formation is dominated by regional mudstone deposits, with sandy gravity flow deposits locally developed in the slope-folding area and submarine plains, and it is the main target for the exploration of ultra-deepwater and ultra-shallow layers in the basin (water depth over 1500 m, and burial depth below the seafloor less than 500 m).

3. Samples and methods

3.1. Sample collection

A total of 14 natural gas samples were collected from 6 wells in the Quaternary Ledong Formation of the QDNB, which were analyzed for natural gas components and carbon isotopes. The locations of the gas sample collection wells are shown in Fig. 1(c). Although only 14 new gas samples were analyzed, these were compared with 33 previously published datasets, and the main interpretations are supported by continuous isotope logging data (~200 points per well across six wells), which together provide sufficient statistical robustness and regional representativeness. Natural gas samples analyzed in this study were obtained through Modular Formation Dynamics Tester (MDT) and Drill Stem Test (DST) operations during drilling. Both methods allow direct sampling of formation fluids at near in-situ pressure and temperature conditions, which effectively minimizes post-recovery alteration of the gas composition. The collected gas was immediately transferred into high-pressure stainless-steel cylinders for storage and transportation, ensuring that the samples remained stable before geochemical analysis.

During MDT sampling, a probe was set against the borehole wall to establish hydraulic communication with the formation, followed by controlled drawdown to extract free gas or dissolved gas released from formation fluids. The sampling was performed under downhole pressure conditions, preventing hydrate dissociation during the process. Similarly, in DST operations, formation gas flowed through the drill stem under controlled bottom-hole pressure, and representative gas samples were taken in sealed cylinders. These procedures ensured that the gas collected reflected the in-situ free gas phase of the reservoir rather than secondary gases released during core recovery or hydrate dissociation.

A key concern in gas sampling is the potential migration of pore gas along the borehole, which could lead to cross-contamination between different depth intervals. To mitigate this, both MDT and DST employed packers and flow isolation systems to hydraulically seal off the target interval during sampling. This design prevented vertical gas flow within the borehole and ensured that the collected gas was solely derived from the specified formation horizon.

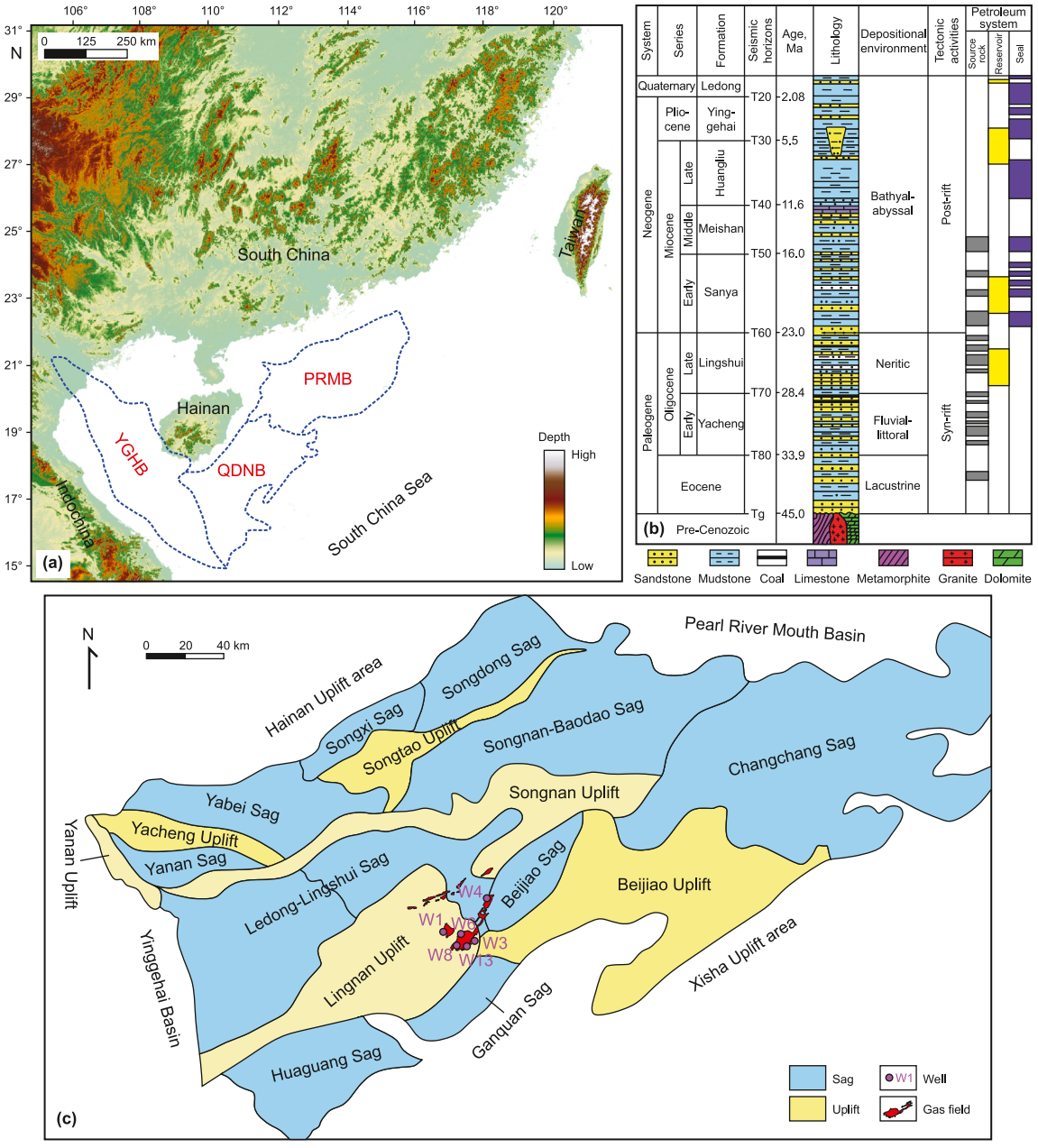

Fig. 1. **(a)** Modern surface elevation map showing the location of the Qiongdongnan Basin (QDNB), Yinggehai Basin (YGHB) and Pearl River Mouth Basin (PRMB) in the South China Sea. **(b)** Comprehensive stratigraphic column diagram of the Qiongdongnan Basin (Lai et al., 2024). **(c)** Regional location and structural divisions of the Qiongdongnan Basin.

3.2. Natural gas component and carbon isotope analysis

Natural gas components and carbon isotopes were measured at the National Key Laboratory of Petroleum Resources and Engineering, China University of Petroleum (Beijing). Natural gas components were analyzed using an Agilent 8890 gas chromatograph (GC) equipped with a flame ionization detector. A capillary column (PLOT Al_2O_3, 27 m × 0.32 mm × 0.25 μm) was used for the separation of individual hydrocarbon gas components from methane to *n*-heptane (C_1–C_8). The initial temperature of the column oven was set at 60 °C and maintained for 1 min. The temperature was then increased to 80 °C at a rate of 20 °C/min, and then to 190 °C at a rate of 30 °C/min for 7 min. Helium was used as the carrier gas at a constant flow rate of 1.0 mL/min.

Carbon isotope analysis was performed using the Trace GC-ISOLINK-MAT 253 IRMS test system. A silica capillary column (HP-PLOT Q 30 m × 0.53 mm × 40 μm) was used to separate the individual alkane gases (C_1–C_5) and carbon dioxide (CO_2). The initial temperature of the chromatogram was 40 °C with a constant temperature of 6 min, and the temperature was increased to 80 °C at 15 °C/min, and then to 200 °C at 5 °C/min with a constant temperature of 5 min. The results were based on the Vienna Pee Dee Belemnite standard ($\delta^{13}C_{VPDB}$ = 0‰) as a reference. Each sample was analyzed three times and the average value was taken with an analytical precision of ±0.5‰.

3.3. Well logs

We employed logging-while-drilling (LWD) data from the six wells mentioned above to interpret lithology and fluid properties. A standard suite of logging curves, including gamma ray, sonic, density, neutron, and resistivity, have been used to infer a range of

reservoir properties such as porosity, gas saturation, and hydrate saturation. These log curves have been corrected for hole size, casing size and drilling fluid type before being interpreted and processed.

3.4. Temperature and pressure measurements

In-situ temperature and pressure profiles were acquired using Schlumberger's Modular Formation Dynamics Tester (MDT) with a Quicksilver Probe module. The measurement principle involves deploying a dual-packer probe to hydraulically isolate the target formation, followed by controlled fluid withdrawal to induce transient pressure-temperature responses. Formation pressures were measured via dual quartz crystal gauges (±0.01 psi accuracy), while temperatures were recorded using platinum RTD sensors (±0.05 °C accuracy), both calibrated against NIST-traceable standards. Depth positioning was validated through gamma-ray log correlation (<0.15 m vertical uncertainty). Pressure data were calibrated against downhole mud weight gradients, revealing a 0.03 (±0.005) psi offset corrected for near-wellbore supercharging, while temperature measurements incorporated transient heat transfer corrections validated against distributed temperature sensing (DTS) baselines. The in-situ temperatures and pressures are subsequently combined with natural gas components and pore water salinity to estimate hydrate phase boundaries (Tishchenko et al., 2005; Riedel et al., 2021).

3.5. Carbon isotope gradient calculation

Continuous methane $\delta^{13}C_1$ profiles (mud gas isotope logging) from six Quaternary hydrate-bearing boreholes were analyzed to quantify vertical isotopic gradients (G), representing the first derivative of carbon isotope composition with respect to depth (Fig. 2(a)). Raw $\delta^{13}C_1$ data were smoothed using a Savitzky-Golay filter to suppress high-frequency noise while preserving trends linked to gas migration. The instantaneous gradient at any depth position z is defined as:

$$G(z) = \frac{d\delta^{13}C_1(z)}{dz} = \lim_{\Delta z \to 0} \frac{\delta^{13}C_1(z+\Delta z) - \delta^{13}C_1(z)}{\Delta z} \quad (1)$$

where z is the vertical depth, m; $\delta^{13}C_1$ is the methane carbon isotope composition at depth z, ‰; $G(z)$ is the vertical methane carbon isotope gradient, ‰/m. This differential approach captures the tangent slope of $\delta^{13}C_1$ variations across lithological boundaries, providing critical insights into gas migration mechanisms. The gradient spectrum reveals two end-member scenarios: (1) $G \to 0$ indicates isotopic homogenization through diffusion-dominated migration, reflecting ineffective capillary sealing and continuous gas leakage (Fig. 2(b)); (2) $G \to \infty$ corresponds to sharp isotopic discontinuities diagnostic of intact capillary seals, where abrupt $\delta^{13}C_1$ shifts mark arrested gas migration and efficient hydrocarbon accumulation.

3.6. Principal component analysis

Principal component analysis (PCA) is a multivariate statistical technique that reduces high-dimensional data into orthogonal components while retaining critical information on variance and covariance structures (Jolliffe and Cadima, 2016). Here, PCA was applied to integrate methane carbon isotope gradients and multi-logging parameters for constructing a composite petrophysical-geochemical proxy. The raw dataset was preprocessed in OriginPro 2023, where all input variables were normalized using the min–max method to a uniform scale of [0, 1], thereby eliminating scale disparities, and outliers beyond three standard deviations ($>3\sigma$) were iteratively removed through Mahalanobis distance filtering. PCA was performed using Origin's built-in multivariate analysis module, which decomposes the covariance matrix via singular value decomposition (SVD) to extract principal components (PCs) (Wold et al., 1987; Abdi and Williams, 2010). Those principal components that retained the ability to explain greater than 80% of the cumulative variance were selected as the integrated logging score, with variable loadings revealing strong correlations between $\delta^{13}C_1$ and logging. Multiple linear regression models were established in Origin, validated by leave-one-out cross-validation, linking the logging-derived score to isotopic signatures. This approach bridges geochemical fingerprints and geophysical logging responses, offering a robust tool for evaluating methane migration and seal capacity.

4. Results

4.1. Petrographic features

The detailed petrography shows that the Quaternary Ledong Formation sediments are composed of skeletal and non-skeletal components, with specific loose-unconsolidated characteristics between them (Fig. 3(a) and (c)). The detrital fraction is dominated by quartz (65%–85% of non-skeletal components), with subordinate feldspar (5%–20%), lithic fragments (5%–20%), and clay minerals (Fig. 3(b), (e)–(i)). Quartz grains display angular to subangular morphologies, suggesting proximal transport. Biogenic constituents are characterized by well-preserved planktonic foraminifera

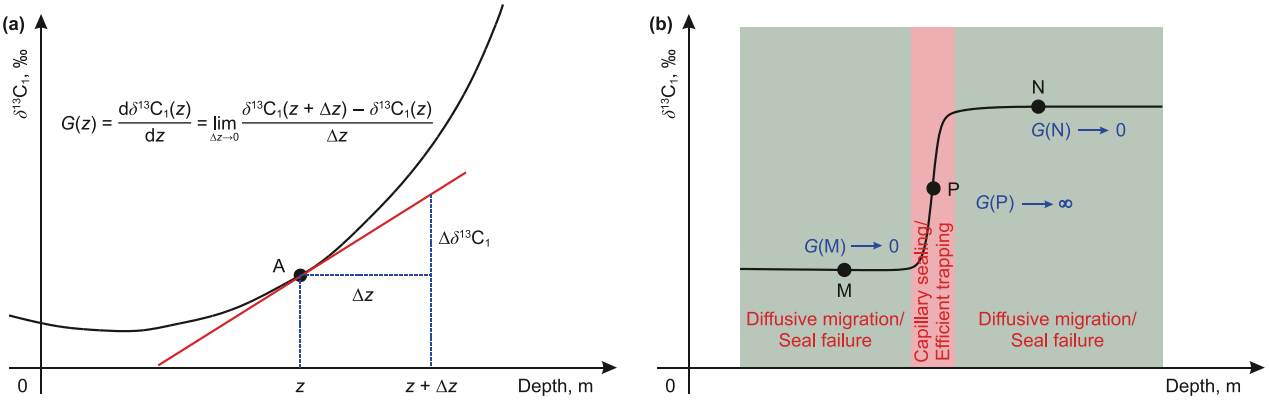

Fig. 2. **(a)** Vertical methane $\delta^{13}C_1$ profile and isotopic gradients. **(b)** Conceptual models linking isotopic gradients to gas trapping efficiency.

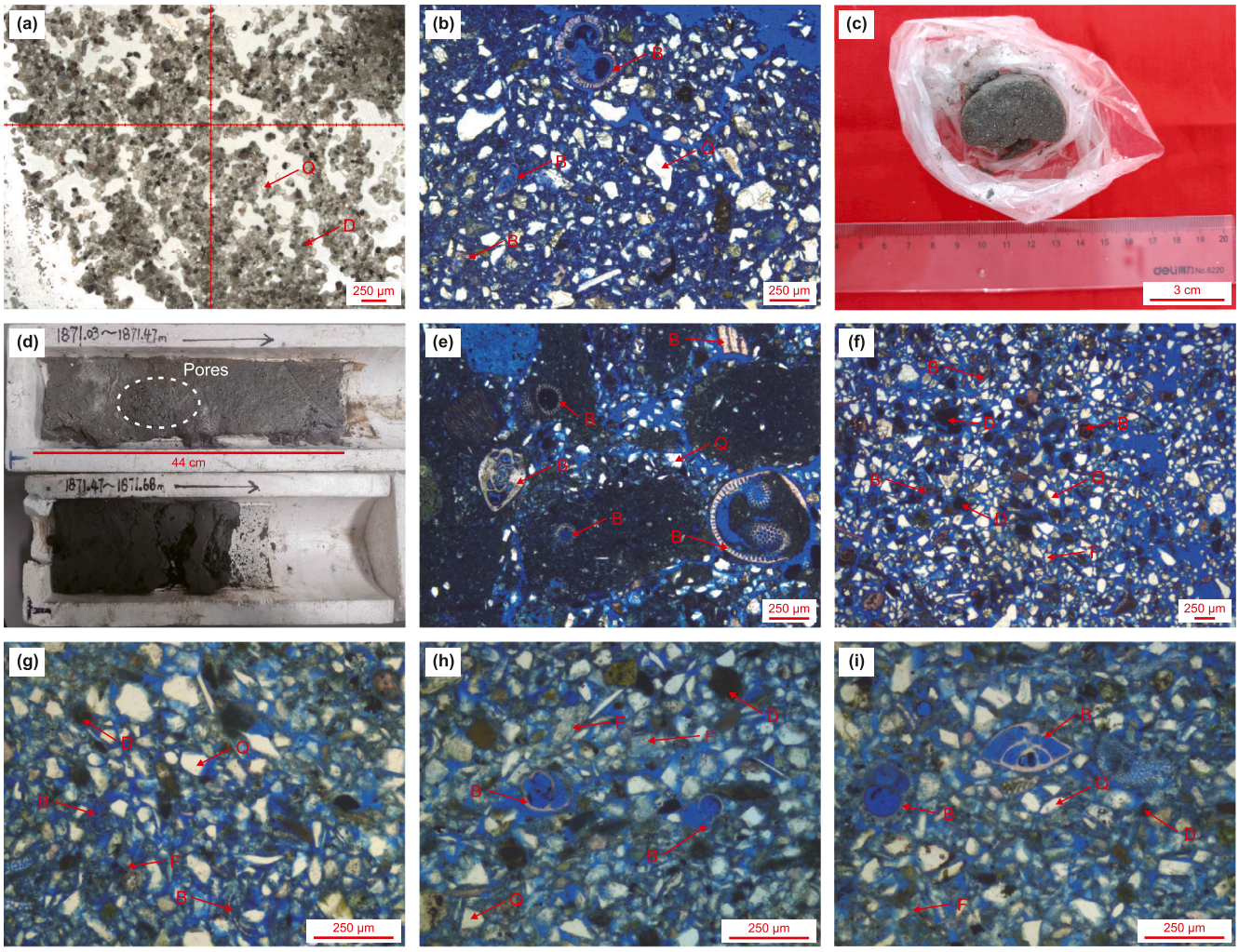

Fig. 3. The photographs showing the different petrographic and mineralogical features observed in the Ledong Formation. **(a)** Well W1, 1826.0 m, fine-grained sandy sediments, washed cuttings; **(b)** Well W1, 1896.0 m, fine-grained sandy sediments, floating or point contacts; **(c)** Well W1, 1902.0 m, loose plug sample, fine-medium grains visible; **(d)** Well W4, 1871.03–1871.47 m, pores remaining after hydrate decomposition; **(e)** Well W4, 1866.5 m, bioclastic debris. **(f)** Well W4, 1871.1 m, fine-grained sandy sediments, floating or point contacts; **(g–i)** Well W6 samples (1766.1 m, 1766.5 m and 1768.7 m) display analogous fine-grained sandy sediments, floating or point contacts between grains. Q: quartz; D: lithic debris; B: bioclasts; F: feldspar.

alongside fragmented bioclasts exhibiting varying degrees of mechanical abrasion (Fig. 3(e)–(i)). The bioclast size spectrum mainly ranges from 50 to 500 μm. Sedimentologically, the formation consists of alternating sandy and muddy sediments. Sandy intervals are predominantly fine-to medium-grained with occasional coarse grains. Grain size analysis reveals moderate to poor sorting. Grain relationships predominantly show floating or point contacts (90%–95% of grain contacts) with minimal compaction-induced deformation. Post-depositional features include hydrate dissociation structures observed in core samples after 72-h atmospheric exposure. These manifest as mm-scale vugular pores with delicate ice-lattice pseudomorphs along pore margins (Fig. 3(d)), suggesting in situ methane hydrate destabilization during core retrieval.

4.2. Geochemical characteristics of natural gas

The composition of natural gases in the study area, dominated by hydrocarbon gases with methane (C_1) contents ranging from 95.7% to 99.6% (mean: 98.2%), exhibits a pronounced dry gas signature (Table 1). This is evidenced by low C_{2+} heavy hydrocarbon content (ethane and propane: 0.02%–0.81%, mean: 0.35%) and high dryness coefficients (C_1/C_{1-5}: 0.98–0.99, mean: 0.99). These compositional characteristics reflect influences from source rock organic matter type, thermal maturity, and potential migration processes.

Carbon isotopic compositions ($\delta^{13}C_1$ and $\delta^{13}C_2$) provide critical insights into gas origins and source rock affinities (Dai et al., 2005; Xiao et al., 2006; Milkov and Etiope, 2018). The $\delta^{13}C_2$ values in the study area range from −24.7‰ to −19.6‰ (mean: −20.9‰), consistent with coal-type thermogenic gases derived from humic organic matter (Table 1 and Fig. 4(a)). However, cross-plots of $\delta^{13}C_1$ versus $\delta^{13}C_2$ and $\delta^{13}C_1$ versus C_1/C_{2-3} reveal a predominance of mixed gas origins (Fig. 4(b)). Specifically, $\delta^{13}C_1$ values (−53.0‰ to −43.8‰) intermediate between deep Huangliu thermogenic gases ($\delta^{13}C_1$: −40.2‰ to −36.8‰) and ultra-shallow microbial hydrate gases ($\delta^{13}C_1$: <−55‰) suggest contributions from both thermogenic and microbial sources (Fig. 4(a)). Notably, well W1 exhibits microbial gas characteristics, suggesting a higher proportion of microbial input relative to thermogenic gas (Fig. 4(b)).

The thermogenic component primarily originates from Yacheng Formation coal-measure source rocks, which are widely

Table 1
Chemical and isotopic compositions of hydrate-related gases, gases in this study area, and deep gases in the QDNB.

Well	Formation	Meter below seafloor (mbsf), m	Natural gas components, %		C_1/C_{2-3}	C_1/C_{1-5}	Carbon isotope composition		References
			C_1	$C_2 + C_3$			$\delta^{13}C_1$, ‰	$\delta^{13}C_2$, ‰	
GMGS5-W08	Ledong	8.0	97.69	2.1	46.5	0.98	−59.5	−26.0	Lai et al. (2021)
		62.9	81.21	17.46	4.7	0.86	−56.3	−26.9	
		148.4	79.16	19.55	4.0	0.85	−50.4	−26.5	
QDNB-08B-2018	Ledong	17.0	97.50	2.0	48.8	0.98	−56.9	−26.6	Wei et al. (2021)
		27.0	90.70	8.5	10.7	0.91	−58.2	−27.2	
		32.7	91.70	7.5	12.2	0.92	−58.8	−28.1	
		60.0	95.60	4.1	23.3	0.96	−62.5	−28.4	
		62.9	85.70	12.8	6.7	0.86	−59.7	−28.4	
		63.7	84.50	14.0	6.0	0.85	−57.2	−27.9	
		63.7	96.70	3.1	31.2	0.97	−63.7	−28.8	
		63.9	89.00	10.0	8.9	0.89	−57.6	−27.9	
		64.5	87.70	11.0	8.0	0.88	−60.0	−29.0	
		64.7	97.20	2.7	36.0	0.97	−61.1	−29.2	
		69.3	88.00	10.6	8.3	0.88	−62.8	−28.7	
		170.2	72.50	23.4	3.1	0.73	−52.0	−27.0	
LS1728	Huangliu	3305.2	89.56	/	/	0.92	−40.2	−25.9	Zhu et al. (2021)
		3406.5	90.82	/	/	0.92	−38.9	−26.0	
LS1724	Huangliu	3251.0	90.23	/	/	0.92	−39.1	−25.4	
		3251.0	90.55	/	/	0.92	−39.0	−25.4	
		3355.0	92.90	/	/	0.98	−39.2	−25.5	
		3445.0	90.64	/	/	0.92	−38.4	−25.8	
SS1721	Huangliu	3306.0	92.51	/	/	0.94	−36.8	−23.5	Huang et al. (2016)
		3324.0	93.25	/	/	0.94	−36.8	−23.6	
		3366.4	92.69	/	/	0.94	−37.3	−23.8	
		3368.5	92.56	/	/	0.94	−36.8	−24.1	
		3321–3351	92.99	/	/	0.94	−37.3	−24.1	
SS1723	Huangliu	3407.0	89.45	/	/	0.93	−37.8	−25.3	
SS1722	Huangliu	3228.5	91.68	/	/	0.94	−38.2	−23.8	
	Huangliu	3331.3	93.04	/	/	0.93	−37.4	−24.2	
SS2211	Huangliu	3339.0	91.12	/	/	0.92	−39.4	−26.2	
		3391.0	91.53	/	/	0.93	−39.2	−26.2	
		3352.5	91.37	/	/	0.93	−38.8	−26.0	
W1	Ledong	263.6–273.2	98.0	0.08	1294.8	0.99	−52.8	−19.6	This study
		263.6–273.2	99.5	0.10	1014.9	0.99	−53.0	−19.7	
		263.6–273.2	98.4	0.12	843.7	0.99	−52.2	−20.0	
W6	Ledong	215.6–225.4	97.7	0.20	485.0	0.99	−47.2	−20.5	
		215.6–225.4	95.7	0.67	142.0	0.99	−46.8	−20.6	
		215.6–225.4	97.8	0.40	244.2	0.98	−46.5	−20.3	
		230.4–240.5	99.6	0.02	4980.0	0.99	−47.2	−20.9	
		230.4–240.5	98.6	0.05	2086.0	0.98	−47.0	−21.0	
		230.4–240.5	96.8	0.04	2518.3	0.99	−47.3	−20.6	
W8	Ledong	217.1–230.2	98.56	0.43	229.2	0.99	−45.3	−21.1	
		217.1–230.2	98.12	0.59	166.3	0.98	−46.9	−23.6	
		217.1–230.2	98.37	0.60	164.0	0.98	−45.4	−24.7	
		217.1–230.2	98.86	0.81	122.0	0.99	−43.8	−19.7	
		217.1–230.2	98.97	0.73	135.6	0.99	−46.7	−20.6	

Note: /, no data.

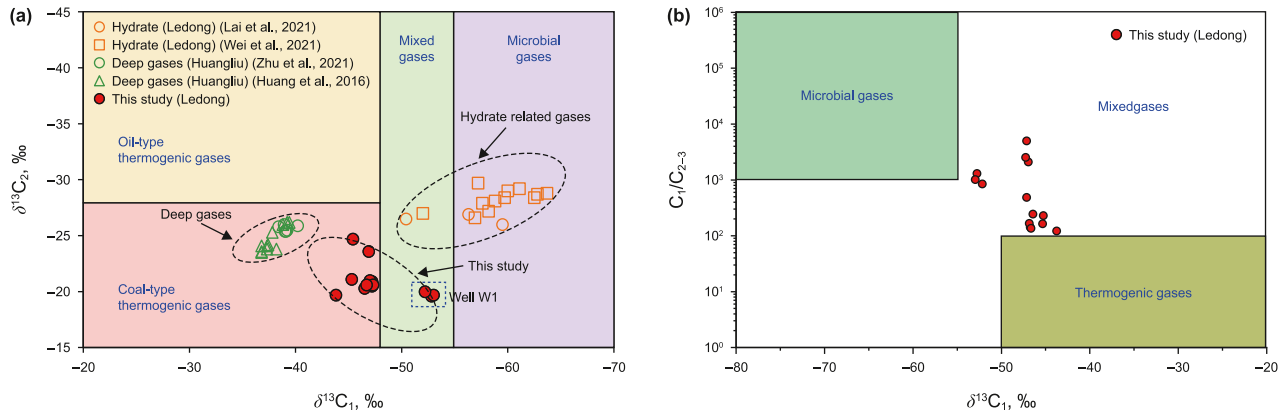

Fig. 4. Genetic diagrams of $\delta^{13}C_1$ versus $\delta^{13}C_2$ **(a)** and $\delta^{13}C_1$ versus C_1/C_{2-3} **(b)** for various gases in the QDNB. The geochemical data of deep gases and hydrate-related gases have been cited in previous studies. See Table 1 for details.

distributed in the QDNB's deep-water regions. These source rocks, characterized by high TOC contents and thermal maturities, have generated substantial coal-type gases that migrated vertically or laterally into shallow reservoirs (Su et al., 2012; Ren et al., 2022; Pei et al., 2024). Microbial activity, typically active at 35–75 °C (Rice and Claypool, 1981; Scott et al., 1994; Stolper et al., 2014), is theoretically constrained to 800–1825 m burial depths under local geothermal conditions (40 °C/km) in the QDNB (Yuan et al., 2009; Zhang et al., 2014). However, the Ledong reservoirs' current burial depths fall outside this microbial window, suggesting limited *in situ* microbial gas generation. Instead, microbial contributions likely derive from biodegradation of pre-existing thermogenic gases or mixing with deeper microbial gases generated in Huangliu-Meishan strata, despite their low TOC contents (Ye et al., 2019; Lai et al., 2022). This multi-source charging system highlights the complexity of gas accumulation processes in ultra-deepwater, ultra-shallow reservoirs.

4.3. Characteristics of the natural gas hydrate stability zone

Integration of in-situ temperature measurements with core-derived pore water salinity values and gas compositional analyses enables precise determination of the methane hydrate phase boundary at the study sites (Fig. 5). At all investigated locations, pore water salinities remain near 35 PSU (Practical Salinity Unit), consistent with normal marine conditions. Seafloor depths across the study area range from 1513.35 to 1616.00 m, with thermal gradients derived from multiple tool deployments showing considerable spatial variation between 42.7 and 56.3 °C/km. These parameters intersect the phase stability boundary for methane hydrate (35 PSU salinity) at depths of 247–347 mbsf (Fig. 5(a)–(f)). At Site W8, while no direct temperature measurements are available, pore water salinity data exhibit comparable characteristics to adjacent sites. We therefore employ the well-constrained geothermal gradient from Site W13 (49.2 °C/km) to model the base of the gas hydrate stability zone (BGHSZ) at this location (Fig. 5(e)). Our analysis reveals two key relationships: (1) BGHSZ depth increases systematically with seafloor depth, and (2) higher thermal gradients reduce BGHSZ depth.

Drilling observations and well-log evaluations demonstrate widespread but heterogeneous hydrate occurrence across the study area. Hydrate-bearing intervals are identified at 6 of 7 sites, with the exception of Site W1 where no significant accumulations were detected. Measured hydrate layers range from 2.3 to 4.7 m thick (mean 3.6 m), substantially thinner than the 247–347 m theoretical stability zone thickness predicted by phase equilibrium modeling. This discrepancy likely reflects multiple controlling factors (a) Low-permeability fine-grained sediments (e.g., clay-rich deposits): act as effective fluid barriers, restricting vertical diffusion fluxes of free gas (Bourg and Ajo-Franklin, 2017; Neuzil, 2019; Hu et al., 2024). This sedimentary architecture promotes preferential hydrate enrichment at chimney tops. (2) Sustained hydrate growth requires prolonged geologic timescales to maintain stable thermal-pressure conditions and continuous gas fluxes (Fisher, 2005; Joye et al., 2005; Kasala et al., 2024). The short sedimentation time of the Ledong Formation in the study area (<0.8 Myr) resulted in the failure to reach phase equilibrium conditions, thus inhibiting the large-scale accumulation of hydrates. (3) Late Quaternary seismic activity (Lüdmann et al., 2001; Shi et al., 2017; Ye et al., 2018) and regional uplift have triggered reorganization of the pressure regime. Such tectonic perturbations not only induce in situ dissociation of preexisting hydrates but also facilitate secondary redistribution through newly generated fluid escape pathways, resulting in dynamic evolution of "non-steady-state" reservoir configurations. These findings align with global statistical patterns of passive margin hydrate systems. Although the base of the gas hydrate stability zone (GHSZ) can be estimated thermodynamically, numerous studies have shown that the actual thickness of gas hydrate accumulations is often significantly smaller than the theoretical stability zone (Klauda and Sandler, 2005; Boswell and Collett, 2011; Ruppel, 2011).

4.4. Methane carbon isotope profile

Systematic variations in methane isotopic composition are observed both vertically and laterally across the study area. The most ^{13}C-depleted methane values (mean $\delta^{13}C_1 = -53.4‰$) are recorded at well W1, while free methane collected from well W4 exhibits the most enriched carbon isotopic signature (mean $\delta^{13}C_1 = -42.5‰$) (Fig. 6). Spatial analysis reveals a systematic northeastward enrichment in methane $\delta^{13}C$ values (−53.4‰ to −42.5‰) along the structural trend. A plot of C_1/C_{2+3} ratios and $\delta^{13}C_1$ values (Fig. 4(b)), combined with $\delta^{13}C_2$ values (Fig. 4(a)), indicates mixing of thermogenic and biogenic methane sources.

The systematic $\delta^{13}C_1$ oscillations (−70‰→−50‰→−70‰) that we highlight in this study are most clearly observed in well W6 (Fig. 6). This well is unique in that continuous downhole isotope logging was obtained across a sufficiently thick interval, thereby recording the complete migration–trapping–remobilization cycle. In contrast, the isotopic datasets from wells W8, W13, W3, and W4 primarily capture thermogenic gas charging and the development of effective top-seals, whereas well W1 mainly reflects thermogenic gas input without subsequent remobilization. The limited depth penetration of most wells (typically ~200–300 m below seafloor) further constrains the vertical coverage of isotope measurements and precludes documentation of the full oscillatory pattern.

Nevertheless, despite these differences in data completeness, the combined isotopic profiles from all wells provide a consistent picture. Taken together, they delineate the critical processes of thermogenic gas input, microbial mediation, and seal formation within a broadly similar depositional–structural framework across the study area. Thus, while well W6 uniquely records the full tripartite $\delta^{13}C_1$ signature, the complementary evidence from other sites reinforces the interpretation that this isotopic oscillation reflects a fundamental, regionally significant cycle of subsurface carbon migration and recycling.

5. Discussion

5.1. Estimation of the proportion of natural gas sources

Natural gas mixing is typically regarded as a physical process wherein chemical composition remains conserved (Schoell, 1983; Snowdon, 2001; Chen et al., 2025). Governed by the principle of mass balance, the stable isotopic composition (e.g., $\delta^{13}C$) of individual components within a mixed-source reservoir is predominantly controlled by their respective isotopic signatures in the contributing end-member gases and the proportions in which they mix. The resultant isotopic value ($\delta^{13}C_{i,M}$) of a specific component "*i*" (e.g., CH_4, C_2H_6) in the mixture (M) can be expressed as a concentration-weighted average (Eq. (2)):

$$\delta^{13}C_{i,M} = \frac{\alpha \times N_{i,A} \times \delta^{13}C_{i,A} + (1-\alpha) \times N_{i,B} \times \delta^{13}C_{i,B}}{\alpha \times N_{i,A} + (1-\alpha) \times N_{i,B}} \quad (2)$$

where *A* and *B* represent the two distinct end-member gases. *i* denotes a specific molecular component (e.g., CH_4, C_2H_6). α is the fractional contribution of end-member A ($0 \le \alpha \le 1$), and $(1-\alpha)$ is

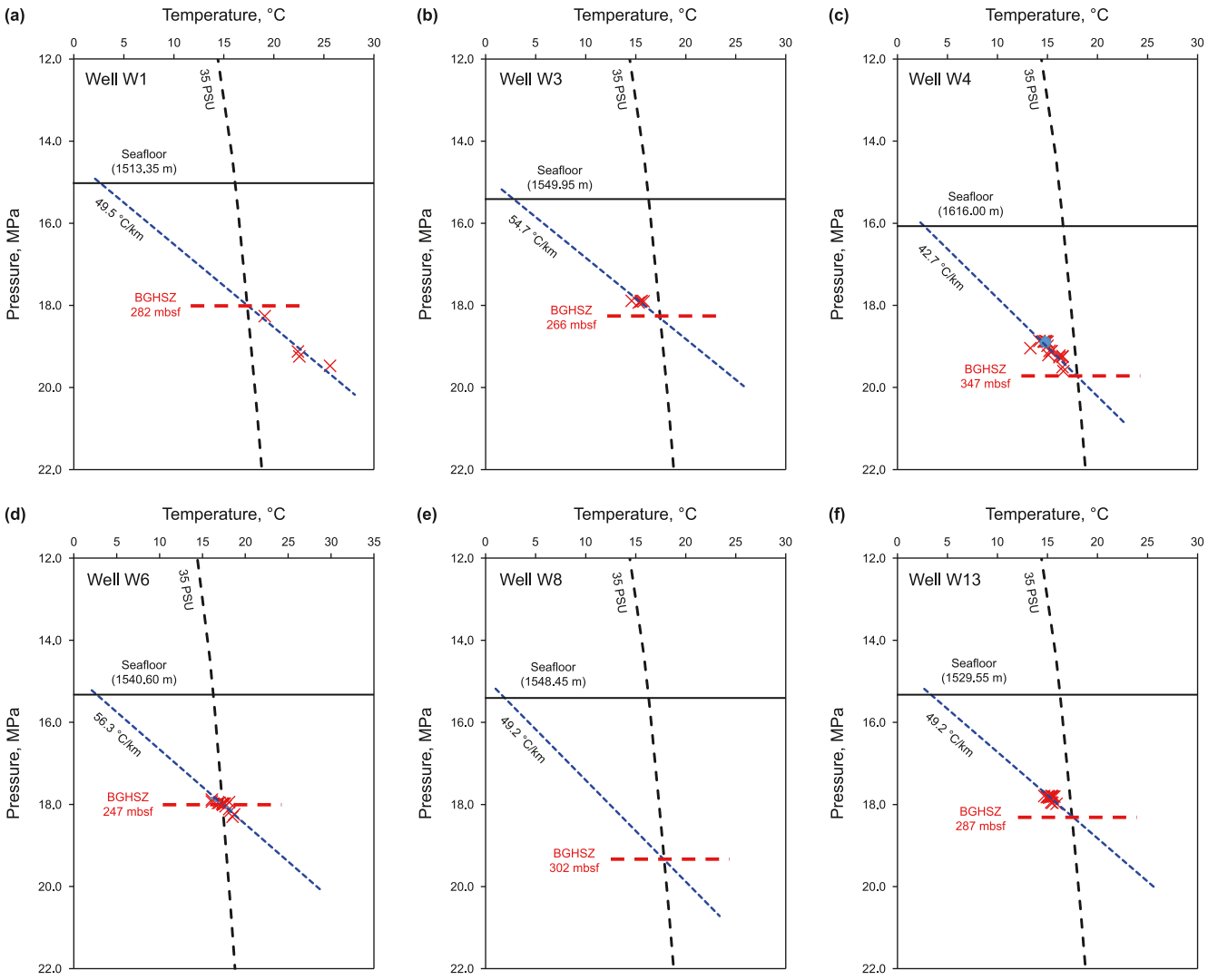

Fig. 5. Calculation of the depth of the base of the gas hydrate stability zone (BGHSZ) at different sites. **(a)** Well W1; **(b)** well W3; **(c)** well W4; **(d)** well W6; **(e)** well W8; **(f)** well W13.

the contribution of end-member B. $N_{i,A}$ and $N_{i,B}$ are the mole fractions (in %) of component "*i*" in end-member gases A and B, respectively. $\delta^{13}C_{i,A}$ and $\delta^{13}C_{i,B}$ are the carbon isotopic compositions (in ‰ VPDB) of component "*i*" in end-member gases A and B, respectively.

This theoretical model provides a viable alternative to complex experimental simulations for quantitatively estimating mixing proportions (α) when the end-member gases exhibit distinct isotopic signatures and possess comparable thermal maturities. However, inherent non-uniqueness (multi-solution potential) exists when applying this model. Different parameter choices (e.g., selecting $\delta^{13}C_1$ vs. $\delta^{13}C_2$) can yield disparate mixing ratios. Consequently, careful consideration of parameter applicability within the specific geological context is paramount. Existing research demonstrates that methane carbon isotopes ($\delta^{13}C_1$) are highly sensitive to thermal maturation effects, making them suitable for discerning mixtures of gases sharing a common source but differing in maturity (Chung and Sackett, 1979; Liu et al., 2019). In contrast, ethane carbon isotopes ($\delta^{13}C_2$) exhibit a stronger inheritance from the original organic precursor, rendering them more effective for quantifying the proportions of mixed gases derived from distinct source types (e.g., terrigenous vs. marine organic matter), particularly when their maturities are similar (Berner and Faber, 1988; Liu et al., 2019).

Integrated analysis of the geological setting, natural gas composition, and carbon isotopic evidence within the Ledong Formation study area reveals a dual-source hydrocarbon charging model dominated by deep thermogenic gas and shallow biogenic gas (Fig. 4). Application of the binary mixing model (Eq. (2)) requires initial characterization of the composition (specifically methane content, C_1) and methane carbon isotopic ratio ($\delta^{13}C_1$) for end-member gases derived solely from each source. Utilizing published data and our own measurements (Table 1), two representative end-member gas samples are selected: a deep gas sample (representative of the Yacheng Formation source rock) and a shallow hydrate-related gas sample (representative of the intra-Ledong Formation source rock). Consequently, the methane content and $\delta^{13}C_1$ values (expressed as averages; Table 2) from these end-members serve as input parameters for the mixing model, enabling quantification of the relative contributions from each source to mixed gases. Finally, based on the $\delta^{13}C_1$ values, an interpretive chart is constructed to estimate mixing proportions within the study area (Fig. 7).

Utilizing the interpretive chart derived from methane carbon isotope values ($\delta^{13}C_1$; Fig. 7), the relative contributions of deep

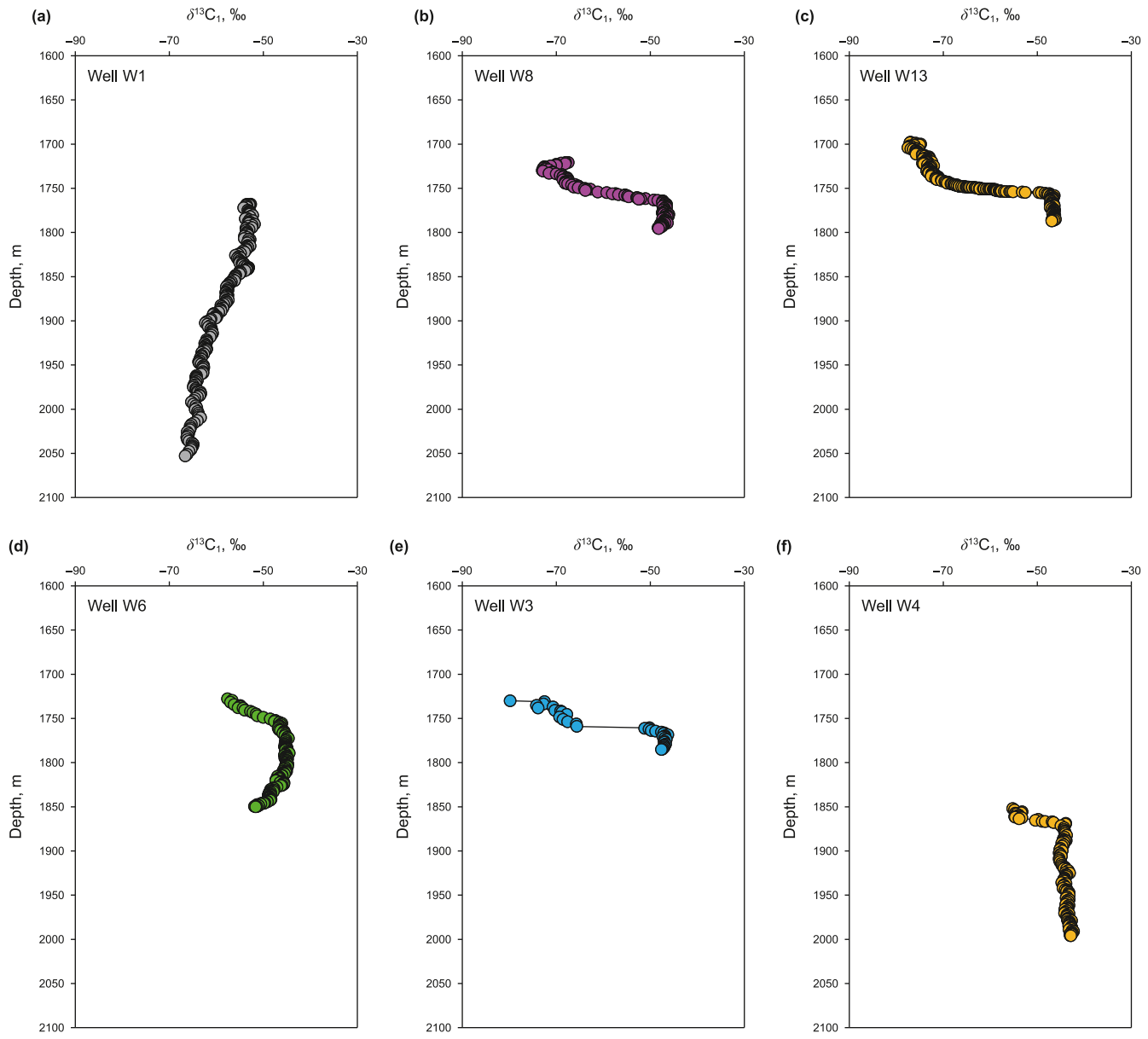

Fig. 6. Methane carbon isotope profiles at different sites. **(a)** Well W1; **(b)** well W8; **(c)** well W13; **(d)** well W6; **(e)** well W3; **(f)** well W4.

Table 2
Composition and carbon isotope characteristics of end-member gases (data from Table 1).

End-member gases	CH_4, %	C_1/C_{1-5}	$\delta^{13}C_1$, ‰	$\delta^{13}C_2$, ‰
Deep gas samples (representative of the Yacheng Formation source rock)	91.58	0.93	−38.3	−25.0
Hydrate related gas samples (representative of the intra-Ledong Formation source rock)	91.01	0.92	−58.7	−27.2

thermogenic gas and shallow biogenic gas to individual reservoirs within the Ledong Formation are quantified. Well W1 gas is predominantly sourced from shallow biogenic gas (68%–72% contribution), while gases from wells W6 and W8 are primarily derived from deep thermogenic sources (55%–73% contribution). It is important to acknowledge the inherent complexity of natural gas mixing. Secondary processes, including isotopic fractionation effects during migration and accumulation, can influence the $\delta^{13}C_1$ values measured in the reservoir (Barker and Fritz, 1981; Zhang and Krooss, 2001; Xia and Tang, 2012). Our application of the binary mixing model did not explicitly account for these potential fractionation effects, which may introduce some uncertainty into the estimated contribution percentages. Despite this limitation, the calculated mixing proportions are broadly consistent with the established geological framework of the study area. This approach provides a valuable quantitative assessment of the relative contributions from distinct sources within the mixed gas accumulations of the Ledong Formation.

5.2. Quantitative evaluation of sealing capacity

Direct in situ measurement of key sealing capacity parameters—such as capillary entry pressure and permeability—in unconsolidated Quaternary sediments containing gas hydrates poses

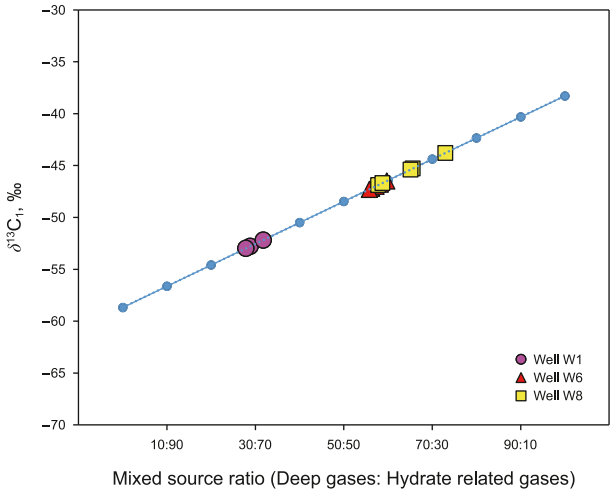

Fig. 7. Carbon isotope characteristics of methane in gases from different source mixtures and analysis of mixed-source ratios.

significant challenges. Furthermore, the complex hydrate growth modes (e.g., cementing, pore-filling, load-bearing) inherent to different reservoir types exert a primary control on pore structure (Waite et al., 2009; Mahabadi et al., 2019), further complicating traditional assessment methods. Critically, the depth gradient of methane carbon isotope ratios ($\delta^{13}C_1$) provides an integrated proxy for sediment sealing capacity, reflecting processes governed by isotopic fractionation during gas migration and retention. To leverage this relationship, we developed a novel quantitative model for sealing capacity evaluation, as demonstrated using well data from the study area (Fig. 8). Firstly, a continuous depth profile of methane $\delta^{13}C_1$ values is constructed from downhole logging measurements. Secondly, the isotopic logging data are smoothed using a Savitzky–Golay filter with a window size of 20 data points and a second-order polynomial, parameters chosen to minimize noise while preserving the primary oscillation features. Thirdly, the first derivative of the smoothed $\delta^{13}C_1$ profile is computed to determine the methane carbon isotope gradient at each depth. Finally, multiple conventional well-log responses (e.g., resistivity, acoustic velocity, density) are integrated using Principal Component Analysis (PCA). This dimensionality reduction technique yields principal component scores and a composite log signature score. A quantitative model for predicting the sealing capacity of unconsolidated, hydrate-bearing sediments is established by calibrating the relationship between the composite log signature score and the methane carbon isotope gradient.

Based on the pre-established gas hydrate stability zone modeling, the study area exhibits potential for hydrate accumulations of variable thickness. Diagnostic well-log responses confirm natural gas hydrate presence through: (1) significantly reduced acoustic transit time (DT), (2) markedly elevated compressional (V_p) and shear wave (V_s) velocities, (3) sharply increased true formation resistivity (RT), (4) slightly decreased bulk density (DEN), (5) low natural gamma ray (GR) values, and (6) a pronounced reduction in V_p/V_s ratio (Moridis et al., 2011; Collett and Lee, 2012; McConnell et al., 2012). Integrated analysis of these diagnostic signatures identifies a 4.75 m-thick gas hydrate interval in well W4 between 1866.00 and 1870.75 m (Fig. 9). The methane carbon isotope gradient peaks at ~1866 m and decreases systematically toward shallower and deeper strata (Fig. 9). This gradient pattern provides indicative evidence of isotopic disequilibrium across adjacent formations, demonstrating effective sediment sealing at this horizon. Furthermore, the downward decline in the methane carbon isotope gradient reveals that the hydrate layer functions as a heterogeneous seal with maximum sealing capacity at its top, progressively weakening downward. This heterogeneity likely reflects controls by hydrate growth modes (e.g., transition from pore-filling to cementing habit) on pore architecture and capillary seal capacity.

Conventional well-log attributes exhibit strong non-uniqueness in subsurface interpretation due to coupled influences from lithology, physical properties, and hydrocarbon saturation. To establish a robust quantitative linkage between standard logging responses and methane carbon isotope gradient variations, we developed an enhanced multi-attribute predictive framework. This framework integrates not only seven key petrophysical parameters—gmma ray (GR), acoustic transit time (DT), bulk density (DEN), true formation resistivity (RT), compressional wave velocity (V_p), shear wave velocity (V_s), and V_p/V_s ratio—but also incorporates their depth-derived gradients (slopes). By transforming all input variables into “rate-of-change” or “gradient” indicators, this approach captures instantaneous responses of different physical properties to the same underlying geological processes, thereby reducing interpretive ambiguity.

Given the significant disparities in measurement units and value ranges among the original parameters and their gradients, direct comparability for Principal Component Analysis (PCA) is precluded. We therefore implemented max-min normalization to standardize all input variables to a uniform [0, 1] scale:

$$X_{i,\mathrm{norm}} = \frac{X_i - X_{i,\min}}{X_{i,\max} - X_{i,\min}} \tag{3}$$

where $X_{i,\mathrm{norm}}$ is the normalized value, X_i is the original measurement (either the raw log value or its depth gradient), and $X_{i,\min}$, $X_{i,\max}$ are the parameter-specific minimum and maximum values across the study interval, respectively. This linear transformation preserves intrinsic data relationships while enabling dimensionally homogeneous feature integration essential for PCA-driven dimensionality reduction.

Following standardization of the 14 resulting variables (7 original parameters + 7 gradient parameters), PCA is performed with cumulative variance explained >85%. The principal component analysis extracted five significant components with eigenvalues greater than 0.7, together explaining 84.02% of the total variance (Table 3). PC1 has the highest eigenvalue (3.10) and accounts for 22.17% of the variance, with strong positive loadings on V_s, V_p, and RT (Table 4). This component integrates acoustic–resistivity attributes and primarily reflects hydrate saturation and pore fluid effects. PC2 explains 21.64% of the variance, dominated by DT, V_p/V_s ratio, and velocity-related slopes (V_p and V_s), indicating elastic property variations and compaction-related lithological controls. PC3 contributes 18.45% of the variance, with high negative loadings on GR, DEN, and V_p/V_s, highlighting clay content and density heterogeneity that affect reservoir quality and hydrate occurrence. PC4, accounting for 16.57% of the variance, is mainly governed by GR, DEN, and V_p/V_s slope parameters, reflecting vertical heterogeneity and seal capacity within hydrate-bearing intervals. PC5, with a smaller contribution of 5.19%, captures higher-order variations through GR, DEN, and RT slopes, which likely represent fine-scale lithological changes and diagenetic effects. Together, these components demonstrate that PC1 and PC2 capture the dominant hydrate-related acoustic–resistivity and lithological controls, whereas PC3–PC5 represent secondary influences from mineral composition, vertical heterogeneity, and localized diagenesis.

Leveraging the component transformation matrix (Table 4), we construct linear equations for the five principal components

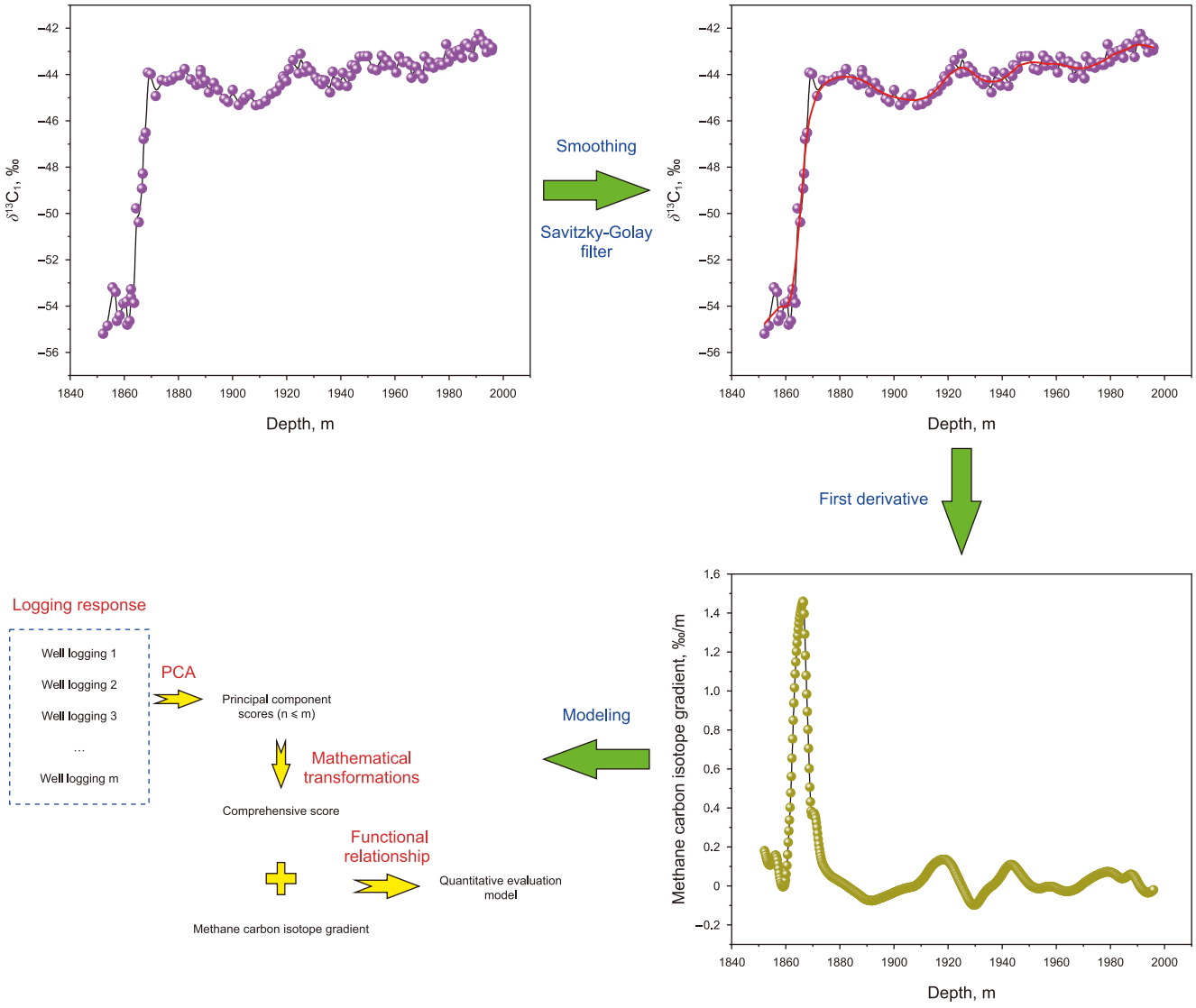

Fig. 8. The procedure of establishing a quantitative evaluation model for sediment sealing capacity based on the methane carbon isotope gradient.

through multivariate regression (Eqs. (4)–(8)). The eigenvalues' variance contributions are then assigned as weighting coefficients to derive a composite scoring function (Eq. (9)). Cross-plot analysis between comprehensive scores and methane carbon isotope gradients across depth intervals demonstrates a robust parametric correlation ($R^2 = 0.7803$) (Fig. 10). Notably, when the comprehensive score exceeds a threshold of 2, the methane carbon isotope gradient increases sharply, suggesting a significant enhancement in sealing capacity. This relationship confirms that conventional well-log attributes and their derivative slope parameters can be quantitatively integrated via PCA into a reliable proxy for methane carbon isotope gradients, thereby enabling predictive assessment of sealing capacity in hydrate-bearing formations.

$$F_1 = -0.1974X_{1,\mathrm{norm}} - 0.3106X_{2,\mathrm{norm}} - 0.1240X_{3,\mathrm{norm}} + \cdots - 0.2035X_{14,\mathrm{norm}} \quad (4)$$

$$F_2 = 0.1626X_{1,\mathrm{norm}} - 0.3036X_{2,\mathrm{norm}} + 0.1862X_{3,\mathrm{norm}} + \cdots - 0.0690X_{14,\mathrm{norm}} \quad (5)$$

$$F_3 = -0.3749X_{1,\mathrm{norm}} + 0.2988X_{2,\mathrm{norm}} - 0.4289X_{3,\mathrm{norm}} + \cdots + 0.1924X_{14,\mathrm{norm}} \quad (6)$$

$$F_4 = 0.1147X_{1,\mathrm{norm}} - 0.2274X_{2,\mathrm{norm}} + 0.0915X_{3,\mathrm{norm}} + \cdots + 0.5029X_{14,\mathrm{norm}} \quad (7)$$

$$F_5 = 0.0017X_{1,\mathrm{norm}} + 0.0252X_{2,\mathrm{norm}} - 0.0251X_{3,\mathrm{norm}} + \cdots - 0.4117X_{14,\mathrm{norm}} \quad (8)$$

$$F_C = 0.2217F_1 + 0.2164F_2 + 0.1845F_3 + 0.1657F_4 + 0.0519F_5 \quad (9)$$

where F_1–F_5: scores of the first to fifth principal components (PC1–PC5), respectively; F_C: composite score (weighted sum of PC scores). $X_{1,\mathrm{norm}}$–$X_{14,\mathrm{norm}}$ represent the min–max normalized values of GR, DT, DEN, V_p, V_s, V_p/V_s ratio, RT, and their respective slope parameters (GR_slope, DT_slope, DEN_slope, V_p_slope, V_s_slope, V_p/V_s_slope, RT_slope).

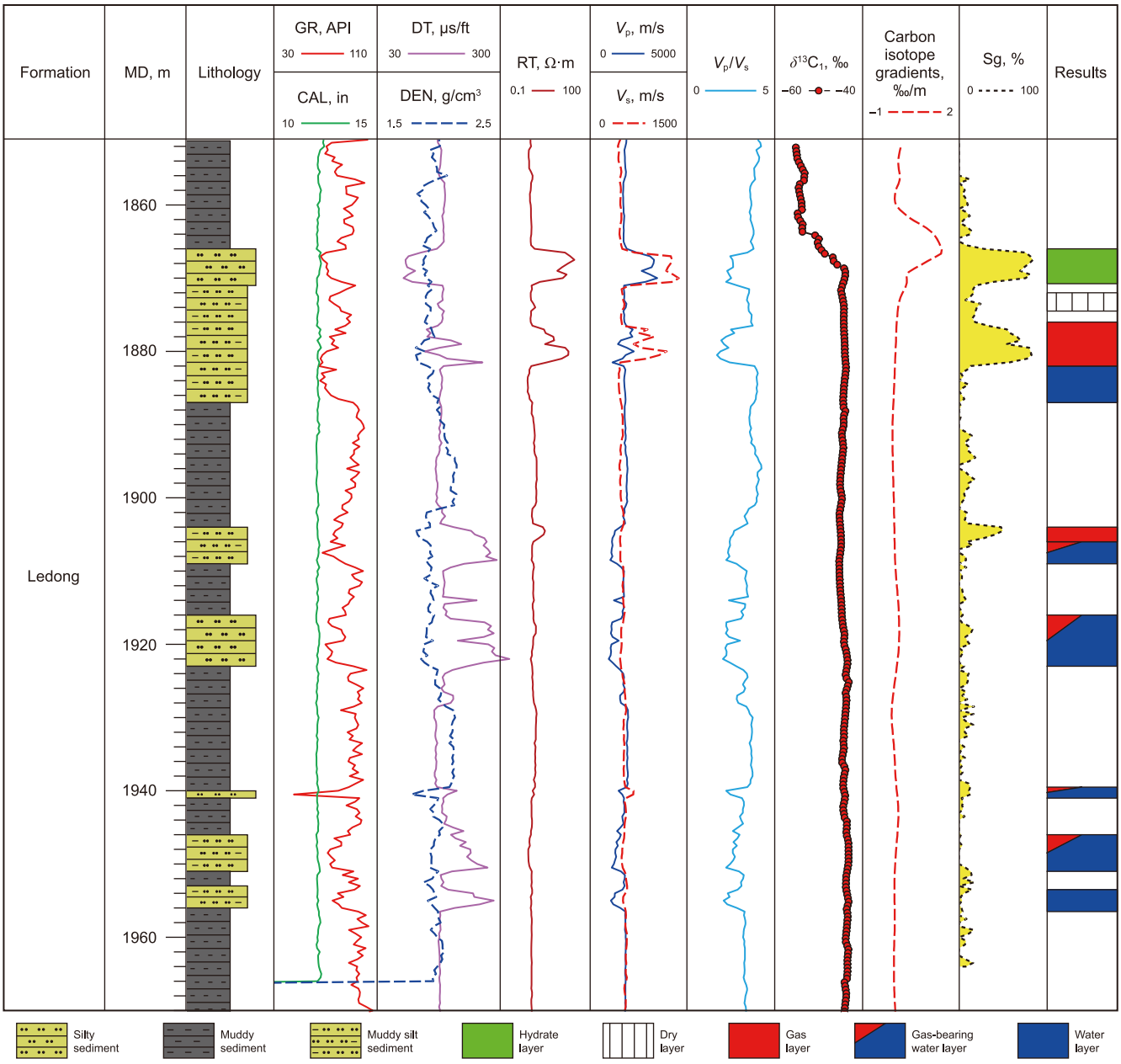

Fig. 9. Logging curves from the W4 drilling site, located at a water depth of 1616.00 m. MD: measured depth; GR: natural gamma ray logging; CAL: caliper logging; DT: acoustic transit time logging; DEN: bulk density logging; RT: true formation resistivity logging; V_p: compressional wave velocity logging; V_s: shear wave velocity logging; Sg: gas saturation.

To further explore the relationship between changes in methane carbon isotope gradients and formation sealing, we compiled methane carbon isotope gradients and corresponding gas saturation data from multiple wells in the study area. The results demonstrate a clear positive correlation, in which intervals with higher $\delta^{13}C_1$ gradients consistently correspond to increased gas saturations (Fig. 11). Notably, when the gradient reaches approximately 0.5‰/m, the gas saturation exceeds 50%, marking a critical inflection point in reservoir performance. This threshold therefore provides a practical diagnostic criterion for distinguishing intervals with effective sealing capacity. Furthermore, the observed consistency between isotopic gradients and gas saturation strongly supports the theoretical link between vertical isotopic enrichment and the suppression of upward gas leakage. Importantly, because $\delta^{13}C_1$ gradients can be predicted indirectly through diagnostic well-log responses and integrated PCA models, this approach offers a novel means of forecasting sealing capacity in unconsolidated, hydrate-bearing sediments where direct core measurements are often unavailable.

5.3. Natural gas accumulation mechanisms and modeling

Mounting evidence identifies marine gas hydrates as a critical climate feedback element sensitive to global warming (Kvenvolden, 1993; Maslin et al., 2010). These metastable deposits exhibit high susceptibility to temperature-pressure perturbations, with potential methane release posing dual threats of accelerated climate forcing and geohazards to offshore operations (Majorowicz et al., 2014; Hassanpouryouzband et al., 2020). Conversely, hydrate formation can enhance sealing capacity,

Table 3
Percentage of variance explained by PCA and eigenvalues of each component.

Principal component number	Eigenvalue	Percentage of variance explained, %	Cumulative percentage of variance explained, %
1	3.10	22.17	22.17
2	3.03	21.64	43.82
3	2.58	18.45	62.26
4	2.32	16.57	78.83
5	0.73	5.19	84.02
6	0.64	4.56	88.58
7	0.59	4.24	92.82
8	0.44	3.11	95.93
9	0.28	2.01	97.94
10	0.19	1.34	99.28
11	0.05	0.39	99.67
12	0.03	0.21	99.88
13	0.01	0.09	99.97
14	0.00	0.03	100.00

Table 4
The loading factors of the indicators associated with each principal component.

Indicators	PC1	PC2	PC3	PC4	PC5
GR ($X_{1,\ norm}$)	−0.1974	0.1626	−0.3749	0.1147	0.0017
DT ($X_{2,\ norm}$)	−0.3106	−0.3036	0.2988	−0.2274	0.0252
DEN ($X_{3,\ norm}$)	−0.1240	0.1862	−0.4289	0.0915	−0.0251
V_p ($X_{4,\ norm}$)	0.4742	0.1086	0.2118	0.0630	−0.0833
V_s ($X_{5,\ norm}$)	0.4226	0.2656	−0.1703	0.2359	−0.0001
V_p/V_s ($X_{6,\ norm}$)	0.5210	0.0291	0.1389	0.1321	0.0251
RT ($X_{7,\ norm}$)	−0.1677	0.2760	−0.4075	0.1175	−0.0469
GR_slope ($X_{8,\ norm}$)	−0.1080	−0.0259	0.1570	0.4090	0.5451
DT_slope ($X_{9,\ norm}$)	0.2016	−0.3665	−0.3183	−0.1926	0.2956
DEN_slope ($X_{10,\ norm}$)	−0.1358	0.0842	0.1574	0.3917	0.5301
V_p_slope ($X_{11,\ norm}$)	−0.0776	0.3820	0.0964	−0.3432	0.3063
V_s_slope ($X_{12,\ norm}$)	−0.1673	0.4370	0.3240	0.0225	−0.2097
V_p/V_s_slope ($X_{13,\ norm}$)	−0.0012	0.4513	0.1578	−0.3270	0.1269
RT_slope ($X_{14,\ norm}$)	−0.2035	−0.0690	0.1924	0.5029	−0.4117

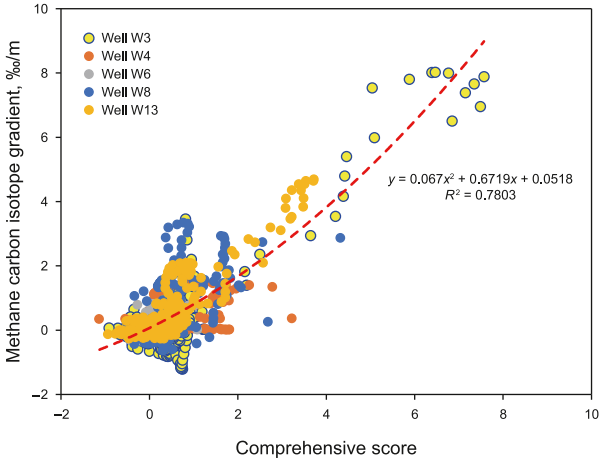

Fig. 10. Crossplot of the comprehensive score obtained from PCA and the methane carbon isotope gradient.

promoting the accumulation of underlying hydrocarbon accumulations. Our study focuses on the Ledong Formation within a deepwater gas hydrate stability zone (Fig. 12(a)). Thermogenic gas migration displays an NE-to-SW vector, with northwestern sectors exhibiting higher thermogenic fractions (55%–73%) (Fig. 7), indicating preferential migration pathways along structural trends.

The effective migration system is the key factor controlling large-scale gas accumulation in the Lingshui 36-1 submarine fan, given that the underlying source rocks have not reached the

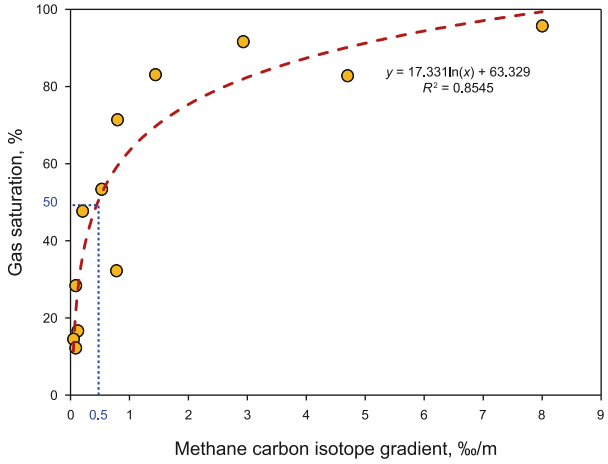

Fig. 11. Crossplot of methane carbon isotope gradient at the top of the gas layer and its gas saturation.

threshold for significant hydrocarbon generation and that the field is located ~35 km laterally and ~4 km vertically away from the gas kitchen of the Yacheng Formation. Since the Neogene, sufficient sediment supply in the western QDNB led to continuous progradation of the shelf break, southward migration of axial canyon systems, and repeated erosion–fill processes of turbidity currents. The subsequent canyon-fill complexes and overspill deposits connected laterally and vertically, forming a relay-like "bowl-shaped" transfer station for gas migration. This transfer station initially accumulated thermogenic gas but was later tilted northwestward due to differential subsidence, creating a "northwest low–southeast high" geometry that favored gas leakage toward the Lingshui 36-1 fan. Consequently, mature thermogenic gas generated in the Yacheng Formation migrated laterally through the canyon-related stacked sand bodies into the Ledong submarine fan (Fig. 13). In addition, local gas chimneys, fractures, and faults in the Lingnan low-uplift area provided vertical pathways for shallow microbial gas to charge the ultra-shallow Ledong fan (Xu et al., 2025). Within the fan, early-stage lower sand bodies were dissected and partially breached, enabling upward redistribution of gas. The overlying mud-rich channels further promoted the development of a NE–SW-trending structural ridge at the fan top, along which gas migrated from the middle-to low-position sand bodies toward the ridge culminations (Fig. 13). Lateral juxtaposition between the Ledong and Yinggehai fans provided favorable migration conditions in the central and eastern fan blocks, whereas migration into the western block was relatively restricted.

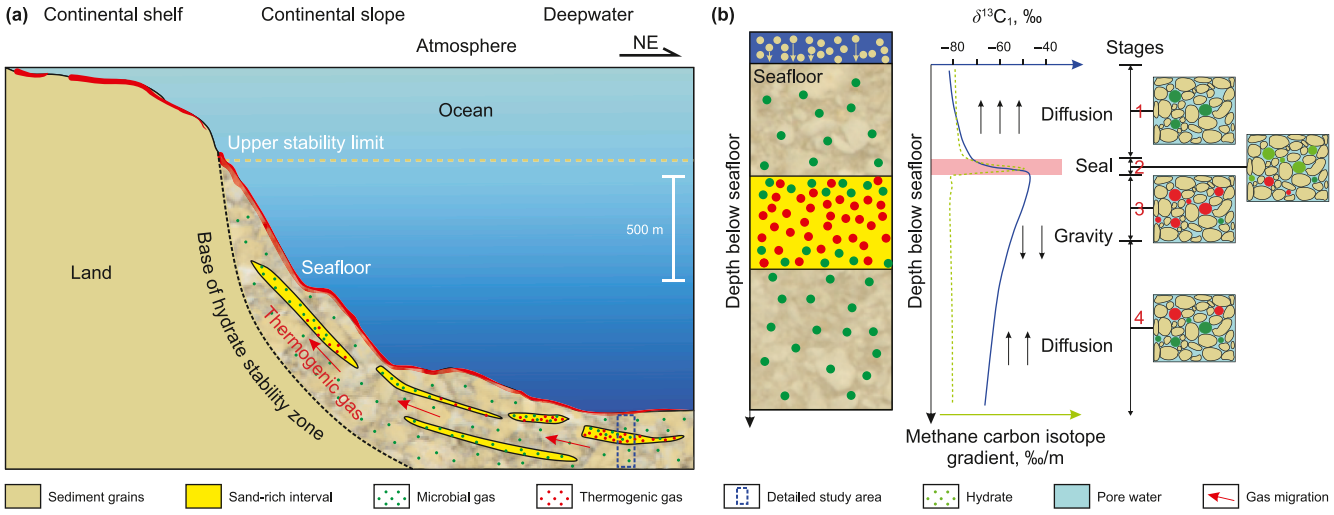

Fig. 12. Methane distribution and main migration directions of thermogenic gas in the study area **(a)** (revised from Ruppel and Kessler (2017)). Conceptual model of gas accumulation through unconsolidated Quaternary hydrate-bearing sediments, and modeled variations in the capillary-dependent methane carbon isotope (solid blue line) and methane carbon isotope gradient (dashed green line) below the seafloor **(b)**. Fig. 12(b) is a further explanation of the position of the dotted blue box in Fig. 12(a).

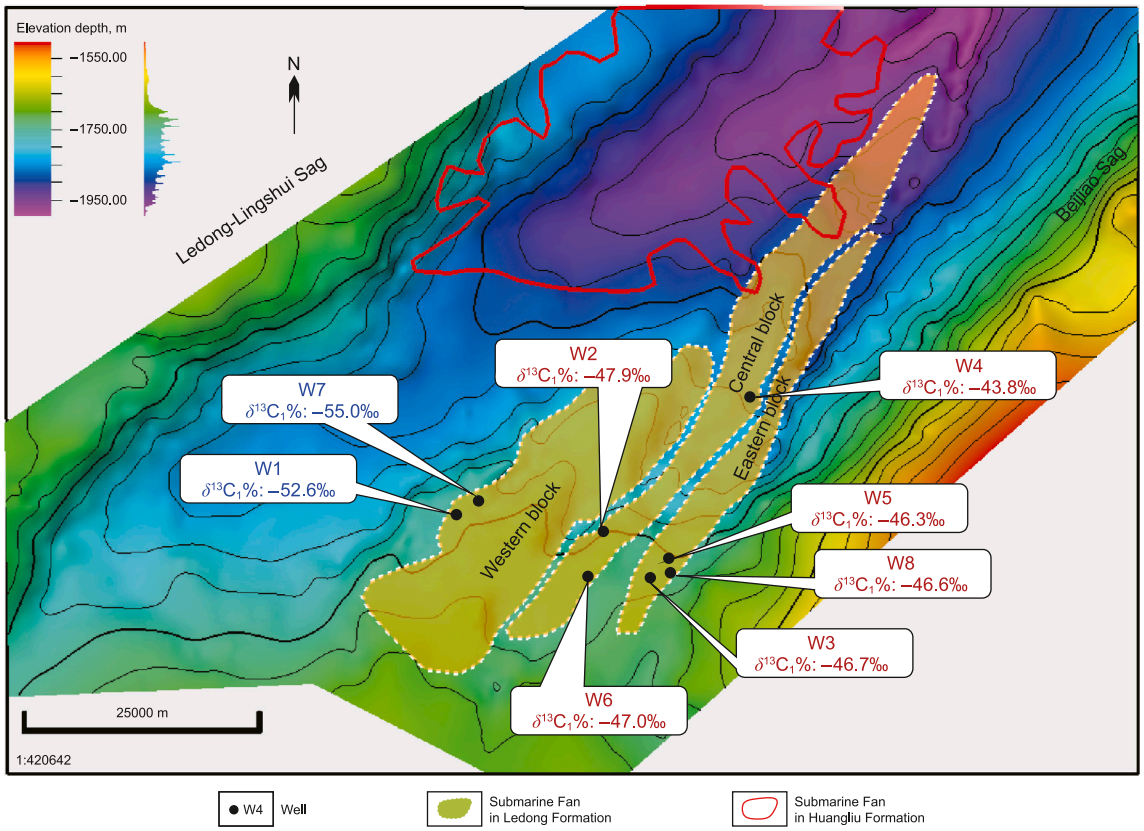

Fig. 13. The top structural map of the Ledong Formation in the study area and the distribution of submarine fans of the Yinggehai Formation and Ledong Formation nearby.

This is supported by methane isotopic values: gases from the western high-position wells (W1, W7) show lighter isotopic values (−66.7‰ to −55.7‰), indicating a dominant microbial origin, while gases from the central and eastern high-position wells (W3, W6) exhibit heavier $\delta^{13}C_1$ values (−47.9‰ to −43.8‰), reflecting a mixed microbial–thermogenic signature. These results confirm that mature thermogenic gas migrated from the central canyon system into the eastern and central fan blocks, consistent with the structural and sedimentary migration pathways delineated from seismic and stratigraphic interpretations.

The methane recycling theory has been proposed to explain the coexistence of enriched hydrate accumulations within the BGHSZ and underlying free gas (You et al., 2019). During sediment burial, hydrates traversing the BGHSZ dissociate into free gas and water (Fig. 12(b)). When gas volumes exceed capillary displacement thresholds, a portion of free gas migrates upward, recycling into

the BGHSZ to form secondary hydrate accumulations—particularly when supplemented by thermogenic gas fluxes. Early models assumed that free gas released by hydrate decomposition would reform hydrates in the BGHSZ (Xu and Ruppel, 1999). Consequently, pore-occluding hydrate layers develop, inhibiting vertical gas migration and promoting further hydrate growth above the BGHSZ. This self-sealing mechanism persists until seal breaching reinitiates free gas flow. Critically, the seal capacity of the caprock is governed by hydrate morphology and saturation, with cementing habits imposing greater flow barriers than pore-filling types.

This study incorporates the mechanism of buoyancy-driven vertical migration of free gas through hydrate-bearing caprocks by analyzing methane carbon isotope ($\delta^{13}C\text{-}CH_4$) signatures and their gradient variations. Vertically, the process can be delineated into four distinct stages (Fig. 12(b)): (1) Stage 1: Pore gas is dominated by microbial methane. Influenced by diffusive fractionation, $\delta^{13}C\text{-}CH_4$ becomes progressively depleted (lighter) upwards, yielding a small positive $\delta^{13}C\text{-}CH_4$ gradient. (2) Stage 2: At the sediment-hydrate interface, extensive hydrate formation within pores creates an effective seal. Beneath this barrier, the influx of thermogenic gas causes $\delta^{13}C\text{-}CH_4$ to increase sharply (become heavier) with depth, producing a pronounced maximum in the $\delta^{13}C\text{-}CH_4$ gradient. (3) Stage 3: Pore gas is primarily thermogenic gas. $\delta^{13}C\text{-}CH_4$ stabilizes near its maximum value, resulting in a near-zero gradient. (4) Stage 4: Mixing occurs between deeper thermogenic gas (migrating under gravity) and shallower diffusing microbial gas. This leads to $\delta^{13}C\text{-}CH_4$ depletion (lighter values) with increasing depth, characterized by a small negative $\delta^{13}C\text{-}CH_4$ gradient. The thickness of this effective sealing barrier ranges from <1 m to tens of meters, contingent upon pore-size distribution and the content of pore water and methane within the sediment. However, rigorous validation of this proposed mechanism requires detailed field observations and/or laboratory experiments focused on the nature and dynamics of the effective barrier.

In the absence of thermogenic gas input, methane carbon isotope ($\delta^{13}C\text{-}CH_4$) values are consistently less than −55.0‰ throughout the profile. Influenced by diffusive fractionation, $\delta^{13}C\text{-}CH_4$ becomes progressively depleted (lighter) upwards with decreasing burial depth. In contrast, the influx of thermogenic gas, facilitated by free gas migration, elevates hydrate saturation, leading to an increase in the thickness of the hydrate-enriched layer. The formation of this hydrate-enriched zone establishes a stable capillary barrier, promoting the accumulation of an interconnected underlying gas column (Fig. 12(b)). Within the effective seal interval defined by this barrier, $\delta^{13}C\text{-}CH_4$ values increase sharply with increasing depth, concomitant with a pronounced maximum in the methane carbon isotope gradient. This isotopic signature reveals disconnected pores and throats within the sealing interval. Notably, not all hydrate-bearing intervals function as effective seals; the effective capillary barrier constitutes only a portion of the hydrate zone. Furthermore, the methane carbon isotope profile indicates that thermogenic gas migration occurs predominantly via lateral pathways.

5.4. Implications for the sealing capacity of unconsolidated hydrate-bearing sediments

Gas hydrate dissociation represents a quantifiable climate risk due to its potential to release vast amounts of methane, a greenhouse gas with 28–34 times the warming potential of CO_2 over a 100-year timescale. Laboratory and numerical studies have shown that each unit volume of hydrate can generate ~164.6 vol of methane gas and 0.87 vol of water under standard conditions, producing rapid pore-pressure buildup and slope destabilization (Nixon and Grozic, 2007). Climate model simulations indicate that seafloor warming of only 2–4 °C could dissociate the entire upper-slope hydrate inventory off the Chilean margin within the next century, potentially releasing several gigatonnes of carbon and triggering slope failure (Alessandrini et al., 2019; Ruffine et al., 2023). Likewise, Arctic permafrost hydrates are highly sensitive to minor warming, with numerical modeling suggesting a lag of merely 20–30 years between the onset of warming and measurable methane release (O'Connor et al., 2010; Thatcher et al., 2013). Although microbial oxidation within sediments and the water column acts as a partial barrier to atmospheric transfer, catastrophic dissociation events such as the Storegga Slide demonstrate that abrupt methane injection into the atmosphere can occur when slope failures bypass these natural filters (Bugge et al., 1988; Maslin et al., 2010). Current estimates suggest that hydrate-related methane emissions may range from 0.1 to 1 Gt C during localized slope failures to several tens of gigatonnes of carbon under regional-scale destabilization, magnitudes sufficient to act as a positive feedback to global warming (Ruppel and Kessler, 2017; Ruffine et al., 2023). Consequently, robust characterization of effective seals and their spatiotemporal sealing capacity is paramount for both hazard mitigation and sustainable resource development. Critically, targeted extraction from well-sealed intervals offers a dual benefit: converting geohazard-prone greenhouse gases into cleaner-burning energy resources while maintaining reservoir stability through controlled depressurization.

Our integrated geochemical and petrophysical analysis reveals that the sealing capacity of hydrate-bearing strata is dynamically recorded in gas composition profiles and methane carbon isotope gradients. Specifically: (1) Thermogenic influx elevates hydrate saturation, promoting capillary barrier formation and underlying gas column accumulation (2) Sharp positive isotopic gradients (e.g., >0.5‰/m). at sediment-hydrate interfaces correlate with effective seals, reflecting arrested vertical migration and isotopic disequilibrium (Figs. 6 and 11). (3) Peak methane carbon isotope gradients (e.g., ~1866 m in well W4) denote zones of maximal pore-throat disconnection, while negative gradients below barriers indicate deeper thermogenic-microbial gas mixing (Fig. 9). These isotopic fractionation patterns provide a direct proxy for seal capacity, with gradient magnitudes scaling with gas saturation. Future studies should integrate core, well log, and seismic attributes to systematically predict spatial heterogeneities in sealing capacity across basin scales. This approach will optimize the identification of high-integrity seals for safer gas extraction and improved assessment of hydrate-associated carbon storage stability.

Although the coupled migration–trapping–remobilization model is established based on data from the Qiongdongnan Basin, its applicability extends beyond the study area. The framework captures fundamental controls—gas charging, isotopic fractionation, and sealing—that are common to hydrate systems worldwide (Milkov, 2005; Collett et al., 2009). Nevertheless, hydrate layers in other regions may originate from different mixtures of microbial and thermogenic gases, and the magnitude of isotopic oscillations depends strongly on local source input and seal integrity. Previous studies in the South China Sea have demonstrated that hydrates are dominantly sourced from microbial methane, with significant thermogenic contributions in fault-controlled or channelized reservoirs (Wu et al., 2011; Zhu et al., 2013; Lai et al., 2021). Therefore, direct application of the model to other basins requires site-specific calibration of gas sources, isotopic baselines, and seal capacity. With such adjustments, the model provides a robust and transferable framework for predicting and evaluating hydrate accumulations in diverse geological settings.

6. Conclusions

This study establishes methane carbon isotope gradients as a robust proxy for evaluating dynamic seal capacity in unconsolidated Quaternary hydrate-bearing sediments of the Qiongdongnan Basin. Key findings reveal:

(1) Vertical methane carbon isotope gradient (>0.5‰/m) quantitatively diagnoses effective capillary barriers within hydrate-bearing strata, with peak gradients correlating to zones of maximal pore-throat disconnection (e.g., 1866 m in well W4).
(2) A quantitative evaluation model for mixed gas sources is established, in which the contribution of thermogenic gas in wells W6 and W8 is 55%–73%, while that in well W1 is 28%–32%. Thermogenic gas influx elevates hydrate saturation, promoting self-sealing through hydrate morphology transitions, which in turn trap underlying mixed gas and form stacked accumulations.
(3) The novel PCA-integrated logging model (cumulative variance: 84.02%, $R^2 = 0.78$) bridges geochemical signatures with petrophysical properties, enabling prediction of seal capacity where direct measurements are unfeasible.

These mechanisms underpin a "charge-dynamic barrier-mixing" model in which the influx of these thermogenic gases that migrate buoyantly, forms dynamic capillary barriers within the hydrate stability zone, trapping underlying microbial gases through buoyancy-driven migration and mixing. This process is documented in diagnostic methane carbon isotope and its gradient profiles, highlighting the dual role of hydrate-bearing sediments as carbon sinks and geohazard sources. Future work should integrate seismic attributes to scale the proxy for basin-wide seal integrity mapping, optimizing both gas hydrate exploitation and climate-risk mitigation in rapidly deposited marginal basins.

CRediT authorship contribution statement

Ya-Zhou Liu: Writing – original draft, Validation, Software, Methodology, Data curation. **Jian-Hui Zeng:** Supervision, Resources, Project administration, Funding acquisition, Conceptualization. **Jun-Cheng Qiao:** Writing – review & editing, Supervision. **Gui-Wen Wang:** Methodology, Formal analysis. **Ke-Liang Dong:** Visualization, Software. **Shu-Ning Liu:** Visualization, Data curation.

Declaration of competing interest

The authors declare that they have no known competing financial interests or personal relationships that could have appeared to influence the work reported in this paper.

Acknowledgments

The authors sincerely thank the Hainan Branch of CNOOC (China) Limited for providing data collection services. This work was financially supported by the Postdoctoral Fellowship Program of CPSF (Grant No. GZC20242002), China, the Science Foundation of China University of Petroleum, Beijing (Grant No. 2462024XKBH005), China, the National Science and Technology Major Project of the Ministry of Science and Technology of China (2025ZD1402707), and the 2021 AAPG Foundation Grants-in-Aid Program (Roger W. Stoneburner Memorial Grant), United States. We thank Editor Min Li and the other two anonymous reviewers for their detailed comments, which significantly improved the manuscript.

References

Abdi, H., Williams, L.J., 2010. Principal component analysis. Wiley Interdiscip. Rev.: Comput. Stat. 2 (4), 433–459. https://doi.org/10.1002/wics.101.
Alessandrini, G., Tinivella, U., Giustiniani, M., et al., 2019. Potential instability of gas hydrates along the Chilean margin due to ocean warming. Geosciences 9 (5), 234. https://doi.org/10.3390/geosciences9050234.
Archer, D., 2007. Methane hydrate stability and anthropogenic climate change. Biogeosciences 4 (4), 521–544. https://doi.org/10.5194/bg-4-521-2007.
Barker, J.F., Fritz, P., 1981. Carbon isotope fractionation during microbial methane oxidation. Nature 293 (5830), 289–291. https://doi.org/10.1038/293289a0.
Berner, U., Faber, E., 1988. Maturity related mixing model for methane, ethane and propane, based on carbon isotopes. Org. Geochem. 13 (1–3), 67–72. https://doi.org/10.1016/0146-6380(88)90026-5.
Boswell, R., Collett, T.S., 2011. Current perspectives on gas hydrate resources. Energy Environ. Sci. 4 (4), 1206–1215. https://doi.org/10.1039/C0EE00203H.
Bourg, I.C., Ajo-Franklin, J.B., 2017. Clay, water, and salt: controls on the permeability of fine-grained sedimentary rocks. Acc. Chem. Res. 50 (9), 2067–2074. https://doi.org/10.1021/acs.accounts.7b00261.
Bray, J.D., Macedo, J., 2023. Performance-based seismic assessment of slope systems. Soil Dynam. Earthq. Eng. 168, 107835. https://doi.org/10.1016/j.soildyn.2023.107835.
Brook, E., Archer, D., Frolking, S., et al., 2008 Potential for abrupt changes in atmospheric methane, pp. 163-201 in U.S. Climate Change Science Program Synthesis and Assessment Product 3.4: Abrupt Climate Change. A Report by the U.S. Climate Change Science Program and the Subcommittee on Global Change Research, U.S. Geological Survey, Reston VA.
Bugge, T., Belderson, R.H., Kenyon, N.H., 1988. The storegga slide. Philos. Trans. R. Soc. Lond., Ser. A Math. Phys. Sci. 325 (1586), 357–388. https://doi.org/10.1098/rsta.1988.0055. https://ui.adsabs.harvard.edu/link_gateway/1988RSPTA.325..357B/.
Cao, H., Jin, S., Hou, M., et al., 2022. Astronomical cycles calibrated the sea-level sequence durations of late Miocene to Pliocene in Qiongdongnan Basin, south China sea. Mar. Petrol. Geol. 143, 105813. https://doi.org/10.1016/j.marpetgeo.2022.105813.
Chen, Y., Jiao, Y., Chen, X., et al., 2025. Quantitative assessment of natural gas geochemical characteristics and mixed source contributions in the Qixia Formation, central Sichuan Basin. Nat. Gas Geosci. 36 (4), 677–688. https://doi.org/10.11764/j.issn.1672-1926.2024.09.004 (in chinese).
Chung, H.M., Sackett, W.M., 1979. Use of stable carbon isotope compositions of pyrolytically derived methane as maturity indices for carbonaceous materials. Geochem. Cosmochim. Acta 43 (12), 1979–1988. https://doi.org/10.1016/0016-7037(79)90010-3.
Collett, T.S., Johnson, A.H., Knapp, C.C., et al., 2009. Natural gas hydrates: A review. AAPG Bull. 93 (6), 809–840. https://doi.org/10.1306/13201142M891602.
Collett, T.S., Lee, M.W., 2012. Well log characterization of natural gas-hydrates. Petrophysics 53 (5), 348–367.
Dai, J., Li, J., Luo, X., et al., 2005. Stable carbon isotope compositions and source rock geochemistry of the giant gas accumulations in the Ordos Basin, China. Org. Geochem. 36 (12), 1617–1635. https://doi.org/10.1016/j.orggeochem.2005.08.017.
Dean, J.F., Middelburg, J.J., Röckmann, T., et al., 2018. Methane feedbacks to the global climate system in a warmer world. Rev. Geophys. 56 (1), 207–250. https://doi.org/10.1002/2017RG000559.
Feng, Y., Qu, A., Han, Y., et al., 2023. Effect of gas hydrate formation and dissociation on porous media structure with clay particles. Appl. Energy 349, 121694. https://doi.org/10.1016/j.apenergy.2023.121694.
Fisher, A.T., 2005. Marine hydrogeology: recent accomplishments and future opportunities. Hydrogeol. J. 13, 69–97. https://doi.org/10.1007/s10040-004-0400-y.
Hassanpouryouzband, A., Joonaki, E., Farahani, M.V., et al., 2020. Gas hydrates in sustainable chemistry. Chem. Soc. Rev. 49 (15), 5225–5309. https://doi.org/10.1039/C8CS00989A.
Hu, G., Zhang, Z., Zhao, Y., et al., 2024. Formation mechanism and geophysical properties of fracture-filling gas hydrate in the host sediments: A comprehensive review. Earth Sci. Rev., 104917 https://doi.org/10.1016/j.earscirev.2024.104917.
Huang, B., Tian, H., Li, X., et al., 2016. Geochemistry, origin and accumulation of natural gases in the deepwater area of the Qiongdongnan Basin, South China Sea. Mar. Petrol. Geol. 72, 254–267. https://doi.org/10.1016/j.marpetgeo.2016.02.007.
IEA, 2024. World Energy Outlook 2024. https://www.iea.org/reports/world-energy-outlook-2024.
Jolliffe, I.T., Cadima, J., 2016. Principal component analysis: A review and recent developments. Phil. Trans. Math. Phys. Eng. Sci. 374 (2065), 20150202. https://doi.org/10.1098/rsta.2015.0202.
Joye, S.B., MacDonald, I.R., Montoya, J.P., et al., 2005. Geophysical and geochemical signatures of Gulf of Mexico seafloor brines. Biogeosciences 2 (3), 295–309. https://doi.org/10.5194/bg-2-295-2005.

Kasala, E.E., Wang, J., Mkono, C.N., et al., 2024. Systematic review and perspectives of methane (CH_4) classifications and production methods from CH4 hydrate reservoirs. Energy & Fuels 38 (20), 19293–19335. https://doi.org/10.1021/acs.energyfuels.4c03427.

Klauda, J.B., Sandler, S.I., 2005. Global distribution of methane hydrate in ocean sediment. Energy Fuel. 19 (2), 459–470. https://doi.org/10.1021/ef049798o.

Kong, W., Wu, C., Zhang, Y., et al., 2025. Fault-driven stress field variations as predictors of bedrock landslide distribution patterns. Landslides 1–20. https://doi.org/10.1007/s10346-025-02475-1.

Kvenvolden, K.A., 1993. Gas hydrates—geological perspective and global change. Rev. Geophys. 31 (2), 173–187. https://doi.org/10.1029/93RG00268.

Lai, H., Fang, Y., Kuang, Z., et al., 2021. Geochemistry, origin and accumulation of natural gas hydrates in the Qiongdongnan Basin, South China Sea: Implications from site GMGS5-W08. Mar. Petrol. Geol. 123, 104774. https://doi.org/10.1016/j.marpetgeo.2020.104774.

Lai, H., Lu, Q., Yang, Z., et al., 2024. Origin and microbial degradation of thermogenic hydrocarbons within the sandy gas hydrate reservoirs in the Qiongdongnan Basin, northern South China Sea. Mar. Petrol. Geol. 165, 106871. https://doi.org/10.1016/j.marpetgeo.2024.106871.

Lai, H., Qiu, H., Kuang, Z., et al., 2022. Integrated signatures of secondary microbial gas within gas hydrate reservoirs: a case study in the Shenhu area, northern South China Sea. Mar. Petrol. Geol. 136, 105486. https://doi.org/10.1016/j.marpetgeo.2021.105486.

Liu, K., Cheng, P., Tian, H., et al., 2023. Development model of shallow lithologic traps and natural gas accumulation mechanisms in marine deep-water areas: a case study in the Qiongdongnan basin, south China sea. Mar. Petrol. Geol. 151, 106211. https://doi.org/10.1016/j.marpetgeo.2023.106211.

Liu, Q., Wu, X., Wang, X., et al., 2019. Carbon and hydrogen isotopes of methane, ethane, and propane: a review of genetic identification of natural gas. Earth Sci. Rev. 190, 247–272. https://doi.org/10.1016/j.earscirev.2018.11.017.

Lüdmann, T., Wong, H.K., Wang, P., 2001. Plio–Quaternary sedimentation processes and neotectonics of the northern continental margin of the South China Sea. Mar. Geol. 172 (3–4), 331–358. https://doi.org/10.1016/S0025-3227(00)00129-8.

Mahabadi, N., Dai, S., Seol, Y., et al., 2019. Impact of hydrate saturation on water permeability in hydrate-bearing sediments. J. Petrol. Sci. Eng. 174, 696–703. https://doi.org/10.1016/j.petrol.2018.11.084.

Majorowicz, J., Grasby, S.E., Safanda, J., et al., 2014. Gas hydrate contribution to late Permian global warming. Earth Planet Sci. Lett. 393, 243–253. https://doi.org/10.1016/j.epsl.2014.03.003.

Marín-Moreno, H., Minshull, T.A., Westbrook, G.K., et al., 2015. Estimates of future warming-induced methane emissions from hydrate offshore west S valbard for a range of climate models. G-cubed 16 (5), 1307–1323. https://doi.org/10.1002/2015GC005737.

Marín-Moreno, H., Minshull, T.A., Westbrook, G.K., et al., 2013. The response of methane hydrate beneath the seabed offshore Svalbard to ocean warming during the next three centuries. Geophys. Res. Lett. 40 (19), 5159–5163. https://doi.org/10.1002/grl.50985.

Maslin, M., Owen, M., Betts, R., et al., 2010. Gas hydrates: past and future geohazard? Philos. Trans. R. Soc. A Math. Phys. Eng. Sci. 368 (1919), 2369–2393. https://doi.org/10.1098/rsta.2010.0065.

McConnell, D.R., Zhang, Z., Boswell, R., 2012. Review of progress in evaluating gas hydrate drilling hazards. Mar. Petrol. Geol. 34 (1), 209–223. https://doi.org/10.1016/j.marpetgeo.2012.02.010.

Milkov, A.V., 2005. Molecular and stable isotope compositions of natural gas hydrates: a revised global dataset and basic interpretations in the context of geological settings. Org. Geochem. 36 (5), 681–702. https://doi.org/10.1016/j.orggeochem.2005.01.010.

Milkov, A.V., Etiope, G., 2018. Revised genetic diagrams for natural gases based on a global dataset of > 20,000 samples. Org. Geochem. 125, 109–120. https://doi.org/10.1016/j.orggeochem.2018.09.002.

Moridis, G.J.J., Collett, T.S.S., Pooladi-Darvish, M., et al., 2011. Challenges, uncertainties, and issues facing gas production from gas-hydrate deposits. SPE Reservoir Eval. Eng. 14 (1), 76–112. https://doi.org/10.2118/131792-PA.

Neuzil, C.E., 2019. Permeability of clays and shales. Annu. Rev. Earth Planet Sci. 47 (1), 247–273. https://doi.org/10.1146/annurev-earth-053018-060437.

Nixon, M.F., Grozic, J.L.H., 2007. Submarine slope failure due to gas hydrate dissociation: a preliminary quantification. Can. Geotech. J. 44 (3), 314–325. https://doi.org/10.1139/t06-121.

O'Connor, F.M., Boucher, O., Gedney, N., et al., 2010. Possible role of wetlands, permafrost, and methane hydrates in the methane cycle under future climate change: A review. Rev. Geophys. 48 (4). https://doi.org/10.1029/2010RG000326.

Passchier, S., 2000. Soft-sediment deformation features in core from CRP-2/2A, Victoria Land Basin, Antarctica. Terra Antartica 7 (3), 401–412. http://hdl.handle.net/10013/epic.28263.d001.

Pei, J., Liu, E., Song, P., et al., 2024. Influencing factors and model of shallow gas enrichment in the Quaternary sediments of the Qiongdongnan Basin, South China Sea. J. Mar. Sci. Eng. 12 (11), 1928. https://doi.org/10.3390/jmse12111928.

Ren, J., Cheng, C., Xiong, P., et al., 2022. Sand-rich gas hydrate and shallow gas systems in the Qiongdongnan Basin, northern South China Sea. J. Petrol. Sci. Eng. 215, 110630. https://doi.org/10.1016/j.petrol.2022.110630.

Rice, D.D., Claypool, G.E., 1981. Generation, accumulation, and resource potential of biogenic gas. AAPG Bull. 65 (1), 5–25. https://doi.org/10.1306/2F919765-16CE-11D7-8645000102C1865D.

Riedel, M., Freudenthal, T., Bialas, J., et al., 2021. In-situ borehole temperature measurements confirm dynamics of the gas hydrate stability zone at the upper Danube deep sea fan, Black Sea. Earth Planet Sci. Lett. 563, 116869. https://doi.org/10.1016/j.epsl.2021.116869.

Ruffine, L., Tang, A.M., O'neill, N., et al., 2023. Environmental challenges related to methane hydrate decomposition from climate change scenario and anthropic activities: state of the art, potential consequences and monitoring solutions. Earth Sci. Rev. 246, 104578. https://doi.org/10.1016/j.earscirev.2023.104578.

Ruppel, C.D., Kessler, J.D., 2017. The interaction of climate change and methane hydrates. Rev. Geophys. 55 (1), 126–168. https://doi.org/10.1002/2016RG000534.

Ruppel, C.D., 2011. Methane hydrates and contemporary climate change. Nat. Educ. Knowled. 2 (12), 12.

Schoell, M., 1983. Genetic characterization of natural gases. AAPG Bull. 67 (12), 2225–2238. https://doi.org/10.1306/AD46094A-16F7-11D7-8645000102C1865D.

Scott, A.R., Kaiser, W.R., Ayers, B Jr., W., 1994. Thermogenic and secondary biogenic gases, San Juan Basin, Colorado and New Mexico—Implications for coalbed gas producibility. AAPG Bull. 78 (8), 1186–1209. https://doi.org/10.1306/A25FEAA9-171B-11D7-8645000102C1865D.

Sellm, M.S., Sloan, E.D., 1990. Hydrate dissociation in sediment. SPE Reserv. Eng. 5 (2), 245–251. https://doi.org/10.2118/16859-PA.

Shi, X., Jiang, H., Yang, J., et al., 2017. Models of the rapid post-rift subsidence in the eastern Qiongdongnan Basin, South China Sea: implications for the development of the deep thermal anomaly. Basin Res. 29 (3), 340–362. https://doi.org/10.1111/bre.12179.

Snowdon, L.R., 2001. Natural gas composition in a geological environment and the implications for the processes of generation and preservation. Org. Geochem. 32 (7), 913–931. https://doi.org/10.1016/S0146-6380(01)00051-1.

Stolper, D.A., Lawson, M., Davis, C.L., et al., 2014. Formation temperatures of thermogenic and biogenic methane. Science 344 (6191), 1500–1503. https://doi.org/10.1126/science.1254509.

Su, A., Chen, H., Feng, Y., et al., 2023. Distal accumulation of leaked gas from deep overpressured zone: the case of the Yanan Sag, Qiongdongnan Basin, South China Sea. Mar. Petrol. Geol. 151, 106181. https://doi.org/10.1016/j.marpetgeo.2023.106181.

Su, L., Zheng, J., Chen, G., et al., 2012. The upper limit of maturity of natural gas generation and its implication for the Yacheng formation in the Qiongdongnan Basin, China. J. Asian Earth Sci. 54, 203–213. https://doi.org/10.1016/j.jseaes.2012.04.016.

Sun, H., Chen, B., Yang, Z., et al., 2022. Natural gas hydrate accumulation mechanisms considering the multi-phase seepage and exploitation disturbance in porous media. Fuel 330, 125687. https://doi.org/10.1016/j.fuel.2022.125687.

Thatcher, K.E., Westbrook, G.K., Sarkar, S., et al., 2013. Methane release from warming-induced hydrate dissociation in the West Svalbard continental margin: timing, rates, and geological controls. J. Geophys. Res. Solid Earth 118 (1), 22–38. https://doi.org/10.1029/2012JB009605.

Tishchenko, P., Hensen, C., Wallmann, K., et al., 2005. Calculation of the stability and solubility of methane hydrate in seawater. Chem. Geol. 219 (1–4), 37–52. https://doi.org/10.1016/j.chemgeo.2005.02.008.

Waite, W.F., Santamarina, J.C., Cortes, D.D., et al., 2009. Physical properties of hydrate-bearing sediments. Rev. Geophys. 47 (4). https://doi.org/10.1029/2008RG000279.

Wei, J., Wu, T., Zhu, L., et al., 2021. Mixed gas sources induced co-existence of sI and sII gas hydrates in the Qiongdongnan Basin, South China Sea. Mar. Petrol. Geol. 128, 105024. https://doi.org/10.1016/j.marpetgeo.2021.105024.

Wold, S., Esbensen, K., Geladi, P., 1987. Principal component analysis. Chemometr. Intell. Lab. Syst. 2 (1–3), 37–52. https://doi.org/10.1016/0169-7439(87)80084-9.

Wu, N., Zhang, H., Yang, S., et al., 2011. Gas hydrate system of Shenhu area, northern South China Sea: Geochemical results. J. Geolog. Res. 2011 (1), 370298. https://doi.org/10.1155/2011/370298.

Xia, X., Tang, Y., 2012. Isotope fractionation of methane during natural gas flow with coupled diffusion and adsorption/desorption. Geochem. Cosmochim. Acta 77, 489–503. https://doi.org/10.1016/j.gca.2011.10.014.

Xiao, X.M., Xiong, M., Tian, H., et al., 2006. Determination of the source area of the Ya13-1 gas pool in the Qiongdongnan Basin, South China Sea. Org. Geochem. 37 (9), 990–1002. https://doi.org/10.1016/j.orggeochem.2006.06.001.

Xu, C., Wu, K., Pei, J., et al., 2025. Enrichment mechanisms and accumulation model of ultra-deep water and ultra-shallow gas: a case study of Lingshui 36-1 gas field in Qiongdongnan Basin, South China Sea. Petrol. Explor. Dev. 52 (1), 50–63. https://doi.org/10.1016/S1876-3804(25)60004-8.

Xu, W., Ruppel, C., 1999. Predicting the occurrence, distribution, and evolution of methane gas hydrate in porous marine sediments. J. Geophys. Res. Solid Earth 104 (B3), 5081–5095. https://doi.org/10.1029/1998JB900092.

Ye, J., Wei, J., Liang, J., et al., 2019. Complex gas hydrate system in a gas chimney, South China Sea. Mar. Petrol. Geol. 104, 29–39. https://doi.org/10.1016/j.marpetgeo.2019.03.023.

Ye, Q., Mei, L., Shi, H., et al., 2018. The Late Cretaceous tectonic evolution of the South China Sea area: an overview, and new perspectives from 3D seismic reflection data. Earth Sci. Rev. 187, 186–204. https://doi.org/10.1016/j.earscirev.2018.09.013.

Yoshimoto, N., Wu, Q., Fujita, K., et al., 2023. Hydrate dissociation and mechanical properties of hydrate-bearing sediments under local thermal stimulation conditions. Gas Sci. Eng. 116, 205045. https://doi.org/10.1016/j.jgsce.2023.205045.

You, K., Flemings, P.B., Malinverno, A., et al., 2019. Mechanisms of methane hydrate formation in geological systems. Rev. Geophys. 57 (4), 1146–1196. https://doi.org/10.1029/2018RG000638.

Yuan, Y., Zhu, W., Mi, L., et al., 2009. "Uniform geothermal gradient" and heat flow in the Qiongdongnan and Pearl River Mouth Basins of the South China Sea. Mar. Petrol. Geol. 26 (7), 1152–1162. https://doi.org/10.1016/j.marpetgeo.2008.08.008.

Zhang, G., Qu, H., Jia, Q., et al., 2021. Passive continental margin segmentation of the marginal seas and its effect on hydrocarbon accumulation: A case study of the northern continental margin in South China Sea. Mar. Petrol. Geol. 123, 104741. https://doi.org/10.1016/j.marpetgeo.2020.104741.

Zhang, G., Zhang, Y., Shen, H., et al., 2014. An analysis of natural gas exploration potential in the Qiongdongnan Basin by use of the theory of "joint control of source rocks and geothermal heat". Nat. Gas. Ind. B 1 (1), 41–50. https://doi.org/10.1016/j.ngib.2014.10.005.

Zhang, J., Yan, D., Pei, J., et al., 2025. Shallow gas accumulation mechanism in the Qiongdongnan Basin, South China Sea. Mar. Petrol. Geol., 107389 https://doi.org/10.1016/j.marpetgeo.2025.107389.

Zhang, T., Krooss, B.M., 2001. Experimental investigation on the carbon isotope fractionation of methane during gas migration by diffusion through sedimentary rocks at elevated temperature and pressure. Geochem. Cosmochim. Acta 65 (16), 2723–2742. https://doi.org/10.1016/S0016-7037(01)00601-9.

Zhao, G., Zheng, J., Gong, G., et al., 2023. Formation characteristics and leakage termination effects of CO2 hydrate cap in case of geological sequestration leakage. Appl. Energy 351, 121896. https://doi.org/10.1016/j.apenergy.2023.121896.

Zhu, H.Y., Dang, Y.K., Wang, G.R., et al., 2021. Near-wellbore fracture initiation and propagation induced by drilling fluid invasion during solid fluidization mining of submarine nature gas hydrate sediments. Pet. Sci. 18 (6), 1739–1752. https://doi.org/10.1016/j.petsci.2021.09.026.

Zhu, W., Shi, H., Huang, B., et al., 2021. Geology and geochemistry of large gas fields in the deepwater areas, continental margin basins of northern South China Sea. Mar. Petrol. Geol. 126, 104901. https://doi.org/10.1016/j.marpetgeo.2021.104901.

Zhu, Y.H., Xia, H., Fu, S.Y., et al., 2013. Gas sources of natural gas hydrates in the Shenhu Drilling Area, South China Sea: geochemical evidence and geological analysis. Acta Geol. Sin.-English Edit. 87 (3), 767–776. https://doi.org/10.1111/1755-6724.12088.